MICROCOPY RESOLUTION TEST CHART

NATIONAL BUREAU OF STANDARDS-1963-A

AD-A173 082

REPORT DOCUMENTATION PAGE

1a. REPORT SECURITY CLASSIFICATION	1b. RESTRICTIVE MARKINGS
UNCLASSIFIED	

2a. SECURITY CLASSIFICATION AUTHORITY	3. DISTRIBUTION/AVAILABILITY OF REPORT
2b. DECLASSIFICATION/DOWNGRADING SCHEDULE	Approved for Public Release; Distribution Unlimited

4. PERFORMING ORGANIZATION REPORT NUMBER(S)	5. MONITORING ORGANIZATION REPORT NUMBER(S)
	AFOSR·TR· 86-0901

6a. NAME OF PERFORMING ORGANIZATION	6b. OFFICE SYMBOL (If applicable)	7a. NAME OF MONITORING ORGANIZATION
Department of Engineering Sciences		AFOSR

6c. ADDRESS (City, State and ZIP Code)	7b. ADDRESS (City, State and ZIP Code)
University of Florida Gainesville, Florida 32611	same as 8c

8a. NAME OF FUNDING/SPONSORING ORGANIZATION Air Force Office of Scientific Research	8b. OFFICE SYMBOL (If applicable) AFOSR/NA	9. PROCUREMENT INSTRUMENT IDENTIFICATION NUMBER F49620-83-K0007

8c. ADDRESS (City, State and ZIP Code)	10. SOURCE OF FUNDING NOS			
Bolling Air Force Base, D.C. 20332	PROGRAM ELEMENT NO.	PROJECT NO.	TASK NO.	WORK UNIT NO.
	61102F	2302	C2	

11. TITLE (Include Security Classification) Dynamic Response of Concrete and Concrete Structures (Unclassified)

12. PERSONAL AUTHOR(S) Malvern, Lawrence E. and Ross, C. Allen

13a. TYPE OF REPORT DRAFT Final Technical	13b. TIME COVERED FROM 821201 TO 860331	14. DATE OF REPORT (Yr., Mo., Day) 30 May 1986	15. PAGE COUNT 58

16. SUPPLEMENTARY NOTATION

17. COSATI CODES			18. SUBJECT TERMS (Continue on reverse if necessary and identify by block number)
FIELD	GROUP	SUB GR.	Concrete, Dynamic Loads, Dynamic Properties, Dynamic Testing, Finite Element Analysis (continued)

19. ABSTRACT (Continue on reverse if necessary and identify by block number)

>This report describes a three-year research program whose objectives were to (1) Develop a loading function for close proximity explosions, (2) Determine dynamic strength properties for selected types of concrete, (3) Incorporate the strength properties so determined into a localized failure criterion for reinforced concrete, (4) Use a structural analysis elastic/plastic finite element computer program to determine localized response for a concrete/steel finite element mesh, and (5) Combine all of these into a simple structural analysis program to determine the response of underground structures to localized impulsive loads. A computational method was developed for calculating the stress transmitted to a buried wall by the pressure wave from a buried conventional explosive of cylindrical shape. Studies were performed on the response of a reinforced concrete structure to such a pressure-wave loading, using several different computer codes and

(continued)

20. DISTRIBUTION/AVAILABILITY OF ABSTRACT	21. ABSTRACT SECURITY CLASSIFICATION
UNCLASSIFIED/UNLIMITED ☒ SAME AS RPT ☐ DTIC USERS ☐	Unclassified

22a. NAME OF RESPONSIBLE INDIVIDUAL	22b. TELEPHONE NUMBER (Include Area Code)	22c. OFFICE SYMBOL
Lt. Col. Lawrence D. Hokanson	202/767-4935	AFOSR/NA

DD FORM 1473, 83 APR	EDITION OF 1 JAN 73 IS OBSOLETE	UNCLASSIFIED

BLOCK 19 (continued)

incorporating some of the preliminary dynamic concrete material property data. The codes have not proved to be effective in predicting the type of response observed in experiments. A new Kolsky apparatus (split Hopkinson's pressure bar system) capable of testing concrete specimens up to 75 mm in diameter was built. The system and procedures are described. References are given to published results, including tests on four kinds of high-strength concrete and on mortar, showing dynamic unconfined compressive strengths up to twice the static values. Additional results on high strength plain concrete and on SIFCON (slurry infiltrated fiber concrete) are reported. Some tentative results from: (1) exploratory dynamic compression of specimens confined by metal jackets, (2) delay times in microcrack initiation and development and (3) lateral inertia in unconfined tests are reported.

BLOCK 18 (continued)

Fracture, Hopkinson Bar, Impact, Kolsky Bar Apparatus, Materials Testing, Rate Effects, Reinforced Concrete Structures, High-Strength Concrete, SIFCON

DTIC

COPY
INSPECTED
1

Accesion For		
NTIS CRA&I	☑	
DTIC TAB	☐	
Unannounced	☐	
Justification		
By		
Distribution /		
Availability Codes		
Dist	Avail and / or Special	
A-1		

DYNAMIC RESPONSE OF CONCRETE AND CONCRETE STRUCTURES

FINAL REPORT

LAWRENCE E. MALVERN

C. ALLEN ROSS

DEPARTMENT OF ENGINEERING SCIENCES

UNIVERSITY OF FLORIDA

GAINESVILLE, FLORIDA   32611

30 MAY 1986

U.S. AIR FORCE OFFICE OF SCIENTIFIC RESEARCH

CONTRACT NUMBER AFOSR F49620-83-K007

UNIVERSITY OF FLORIDA

86 10   6 067

PREFACE

This is the final technical report on a three-year program of research sponsored by the U. S. Air Force Office of Scientific Research, Directorate of Aerospace Sciences, Bldg. 410, Bolling Air Force Base, D. C., 20332. Program Manager for the Air Force is Lt. Col. Lawrence D. Hokanson. This final report describes the technical effort during the period from 1 December 1982 through 30 May 1986.

The contractor is the University of Florida, Division of Sponsored Research, 219 Grinter Hall, Gainesville, Florida 32611. The research was performed by personnel of the Department of Engineering Sciences, University of Florida, Gainesville, Florida, 32611, at the Gainesville campus of the University and at the University of Florida Graduate Center, Box 1918, Eglin Air Force Base, Florida, 32542-0918. Co-Principal Investigators are Professor Lawrence E. Malvern at the Gainesville campus and Professor C. Allen Ross at the Eglin Graduate Center.

TABLE OF CONTENTS

LIST OF FIGURES

LIST OF TABLES

SECTION I

INTRODUCTION

A better understanding of the dynamic response of concrete and concrete structures to impulsive loadings is urgently needed as a foundation on which to base both designs for adequate protective structures and plans for munitions that can defeat protective structures. This final report describes a three year fundamental research program investigating three major areas in order to contribute to a better understanding of the dynamic response. These three areas are (1) determination of the loads applied to a structure by a close-in conventional explosion, (2) strength properties of concrete at the high loading rates induced in a structure by a close-in conventional explosion, and (3) localized dynamic structural failure criteria.

A two-part investigation was addressed to these areas. Task I was an extension of previous studies at the University of Florida on structural response, while Task II addressed the material response by developing a new test facility to measure the compressive stress-strain response of concrete in the strain-rate range from 5 sec^{-1} to 1000 sec^{-1} and modeling the dynamic behavior. The two tasks were pursued concurrently.

The objectives of Task I were to:

1. Search literature and consult with other agencies in order to develop a loading function for the loads on structures resulting from cylindrical charges of arbitrary orientation,
2. Use a structural analysis elastic/plastic finite element computer program to determine early time localized response for a concrete/steel finite element mesh,
3. Search literature for dynamic localized failure criteria and possibly develop a new criterion,
4. Obtain better estimates of dynamic properties of concrete from the results of Task II of this program, and
5. Combine all the above into a simple structural analysis program to determine response of underground structures to intense impulsive loads.

The research on Task I was directed by Prof. C. A. Ross. Results of this research are reported in Section II.

The over-all objective of Task II was to develop representations for the dynamic response of concrete that can be incorporated into structural codes. Since very little experimental information was available on the material response at strain rates above about 5 sec^{-1}, a new test facility was built for dynamic compressive testing at strain rates up to 1000 sec^{-1}. An existing Kolsky Apparatus, a split Hopkinson's Pressure Bar (SHPB) with 3/4-inch (19.05 mm) diameter specimens was used to test mortar with sand particles of maximum diameter 2.36 mm (1/8 the specimen diameter). For concrete with larger aggregate a new SHPB was built to accomodate specimens up to 3 inches (76.2 mm) in diameter. The testing program on mortar was undertaken mainly for guidance in planning the new facility for concrete.

Section III of this report includes some background on dynamic testing, describes the new system and procedures, and reports results obtained with it of unconfined dynamic tests on five types of high-strength concrete with

1

coarse aggregate maximum sizes up to 12.5 mm. At failure strain rates from about 5 sec^{-1} to 120 sec^{-1}, significant increases in unconfined compressive strength over the static strength have been confirmed. Some exploratory investigations have also been made of confined dynamic compressive tests, of delay times in microcrack initiation and development in unconfined tests, and of lateral inertia effects in unconfined tests; preliminary results are presented in Section III.

Summaries and conclusions of the two investigations under Task I and Task II are presented in Section IV. References cited in Sections II and III are listed in Section V at the end of the report.

SECTION II

TASK I: FINITE ELEMENT CALCULATIONS, LOADING FUNCTION MODEL AND LOCALIZED DYNAMIC SHEAR FAILURE MODEL

2.1 Loading Function Model

2.1.1 Introduction

The loading of buried structures from close in and very localized underground explosions is discussed in many documents too numerous to list. Some of them were referenced in the First and Second Annual Reports of this study (References 1 and 2). Much of the literature is concerned with presentation of experimental data and empirical relationships relating pressures in soils at some distance from the source. The scatter in the experimental data is very large, and measurements of pressures, particle velocities, wave speed, etc., in both field and laboratory have shown variations as much as ± 60 percent. These variations are present and must be considered in testing and analysis of structural response.

A structural test using buried explosives should be considered to be in doubt in the same manner as an analysis using the pressure loading calculated from the empirical equations. Much of the data on pressure loading from underground explosions is based on measurements made at normal incidence, and relations for other than normal incidence are necessary to determine pressures on inclined surfaces. In the case of spherical pressure waves impinging on flat surfaces, the wave front reaches the surface at other than normal incidence at all points other than the points of the surface nearest to the source. Hydrodynamic calculations of an explosion in sand (Reference 3) show that, for intense pressures, reflection coefficients at normal incidence and at other than normal incidence may be greater than the usually assumed 2.0 value. However, numerical calculations of Reference 4 for less intense explosions show a 45°-50° cone of rather high pressures and pressures falling off to much lower values out beyond that conical region.

For underground explosions where soil/concrete interfaces are present, the ratio of the dilatation wave speeds of the two media is approximately 4 or 5. From simple wave mechanics, regular reflection and refraction relations break down when the incident angle exceeds the critical angle, which makes the refraction angle $\pi/2$. Snell's law shows that this occurs for incidence at approximately 15° to the normal for a dilatational wave speed ratio of 4.0. At the critical incident angle the refracted wave separates from the reflected and incident wave and runs out ahead of these waves at the wave speed in the concrete. In optics this phenomenon is defined as total reflection, and for planar waves a total reflection is known to occur. However, for spherical or cylindrical waves, the reflection/refraction process is complicated by interface refracted head waves which trail back from the refracted wave and are tangent to the reflected waves. Effects of this phenomenon are present in the calculations of a sand/concrete interface in Reference 4 and are also shown photoelastically in the two bonded dissimilar birefringent materials of Reference 5. Both sets of data show a cone of 45°-50° of rather high stress with reduced stresses beyond the 45°-50° area.

In an effort to account for the reflection at other than normal incidence the authors presented a model in the Second Annual Report of this Study (Reference 2). This model neglects the effects of the surface refraction wave

which runs out ahead of the reflected wave and treats the incident wave as a second order tensor. The transmitted or refracted wave is then based on the normal to the interface surface. This model is reviewed in the next section.

2.1.2 Cylindrical Explosive Loading Function

The loading function as described in Reference 2 is reviewed here in order that it be included in this report. A schematic of the cylindrical explosive is shown in Figure 1. The nomenclature and symbols used in this model are

$$x_i = (x - X_1) - (X_2 - X_1)(i - 1/2)/N$$

$$y_i = (y - Y_1) - (Y_2 - Y_1)(i - 1/2)/N$$

$$z_i = Z_1 + (Z_2 - Z_1)(i - 1/2)/N$$

$$R_i = (x_i^2 + y_i^2 + z_i^2)^{1/2}$$

$N =$	Nearest odd integer to (L/D)
X_1, Y_1, Z_1	Location of explosive ends
X_2, Y_2, Z_2	$Z_2 > Z_1, \quad Y_2 > Y_1, \quad X_2 > X_1$
t_{01}	Time of arrival of first pressure pulse from the first element $i = 1$, time zero for structural response
t_{0i}	Time of arrival of pressure pulse from ith element
Δt_i	Pulse length of pressure pulse from ith element
$\sigma(x_i, y_i, t_i)$	Pressure time function of pressure pulse from ith element at a point (x,y)
$F(t_i)$	Time function for a pressure pulse of ith element at a point (x,y)
$\sigma(x_i, y_i)$	Spatial function for a pressure pulse of ith element at a point (x,y)
α	Time decay constant for pressure time curve
K	Coefficient of pressure term (Ref. 6)
η	Attenuation coefficient (Ref. 6)
$\rho_s c_s$	Soil characteristic impedance
W	Explosive weight
σ_T/σ_I	Transmission ratio, ratio of characteristic impedances for soil/concrete interface (Ref. 2)
k_t	Transverse pressure coefficient (Ref. 2)

4
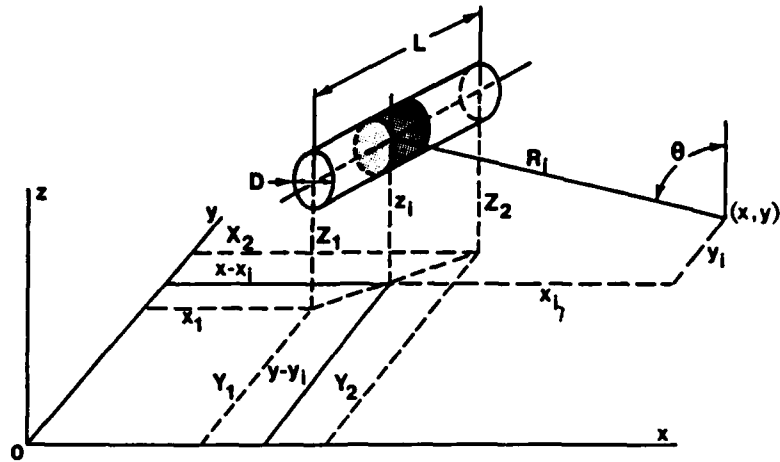
Figure 1. Schematic of Cylindrical Explosive.

From Reference 2 the reflected pressure at point (x_i, y_i) is given as

$$\sigma(x_i, y_i) = K\rho_s c_s [(W/N)^{\eta/3}](\sigma_T/\sigma_I)[(1 - k_t)(z_i^2/R_i^{\eta+2}) + k_t/R_i^{\eta}]. \tag{1}$$

The stress σ at (x_i, y_i) at time t_i is assumed to be given by a separated-variable function

$$\sigma(x_i, y_i, t_i) = \sigma(x_i, y_i) F(t_i) \tag{2}$$

where $F(t_i)$ is given as

$$F(t_i) = [1 - (t - t_{0i})/\Delta t_i] \exp [- \alpha(t - t_{0i})/\Delta t_i]$$

for $\quad (R_i - z_1)/c_s \leqq t \leqq (2R_i - z_1)/c_s \tag{3}$

and $\quad F(t_i) = 0$

for $\quad (R_i - z_1)/c_s > t > (2R_i - z_1)/c_s$

The arrival time t_{0i} is measured from the arrival time of the first pressure pulse at $(x_1, y_1, 0)$. The pulse duration is also assumed to be a function of pulse arrival time, based on experimental evidence of Reference [6]. For these asumptions the pulse duration and arrival time become

$$t_{0i} = R_i/c_s$$
$$\Delta t_i = R_i/c_s \tag{4}$$

The first term of Eq.(4) above is in error in Reference 2. These two items of Eq.(4) then set the range of time given in Eq.(3). Use of Eqs.(1),(2),(3) and (4) gives the stress transmitted to a structure at a point (x,y) at time t as

$$\sigma(x, y, t) = \sum_{i=1}^{N} \sigma(x_i, y_i, t_i) \qquad (5)$$

This model has been inserted in the NONSAPC (Reference 13) finite element code used in References 1 and 2 and Section 2.2 of this report.

2.2 Shear Response of Concrete and Reinforced Concrete Slabs

2.2.1 Introduction

The dynamic response of concrete and reinforced concrete slabs to very localized loading such that failure occurs away from the edges of the slab and prior to the beginning of flexural response is covered in some detail in Reference 7. For this reference failure is assumed to occur when the applied impulse occurring within a specified time exceeds a critical impulse. The specified time is assumed to be the quarter period of the flexural response, and the critical impulse is based on the critical velocity required for complete through-the-thickness failure of the concrete slab.

In this report and in References 7 and 8, shear failure is defined to mean that a portion of the concrete slab situated away from the edges is separated from the remainder of the slab. A study in Reference 9 is concerned with direct shear of a slab at the edges when the entire slab is loaded as a function of time. For the Reference 9 study the initial loading is uniform but due to slab displacement a reduction of loading near the midpoint is experienced. This reduction in loading pressure near the center is defined as soil arching in Reference 10. In Reference 9 a single degree of freedom method using a Timoshenko beam analysis is applied to a wide beam. In this case shear at the beam ends was examined for complete edge severance. Results of the Timoshenko beam analysis are displayed by a ratio of edge-shear/ultimate-shear versus time. Shear failure is assumed to occur first if the shear ratio curve crosses unity prior to that of the bending ratio curve. For this analysis edge effects play an important part in the response and some edge stiffness must be assumed.

For shear failure of a slab far from the edges, edge effect plays no part in the analysis, since shear failure is assumed to occur prior to flexural response. In this study two additional methods which will be applicable to concrete and reinforced concrete slabs will be discussed in terms of failure of concrete, failure of concrete reinforcing elements and failure of concrete between the reinforcing elements.

2.2.2 Critical Impulse Method

The critical impulse method is described in some detail in References 7 and 8 and is reviewed here.

Based on a method of Reference 11 a critical velocity for through-the-thickness shear of a concrete or reinforced concrete slab is given as

6

$$v_{cr} = \frac{2\sqrt{2}}{3} \left(\frac{\sigma_u}{\rho}\right)^{1/2} \tag{6}$$

where $\quad v_{cr}$ = the critical velocity

σ_u = the ultimate tensile strength

ρ = density.

A relationship for velocity and impulse may be written as

$$I_{cr} = \rho h v_{cr}, \tag{7}$$

where h is slab thickness. By using a linear rule of mixtures for σ_u and ρ the critical impulse I_{cr}, required for shear failure, may be written as

$$I_{cr} = \frac{2\sqrt{2}}{3} h \left\{ [(1 - q)\rho_c + q\rho_s] [(1 - q)(0.13)f'_c + q(1.25)\sigma_s] \right\}^{1/2}, \tag{8}$$

where $\quad$ h $\quad$ = slab thickness

ρ_c $\quad$ = concrete density

ρ_s $\quad$ = reinforcement density

σ_s $\quad$ = reinforcement tensile strength

q $\quad$ = total reinforcement ratio (top and bottom, one direction, plus shear reinforcement)

f'_c = static compressive strength

The constant 0.13 of Eq. (8) represents a combination of 1.3 dynamic increase factor and 0.1 of f'_c for tensile concrete strength. The 1.25 constant of Eq. (8) represents a dynamic increase factor for steel reinforcement. These two dynamic increase factors are rather arbitrary but appear to be reasonable for the simplified analysis.

The applied specific impulse I_{ap} is determined from the equation

$$I_{ap} = \left(\frac{2}{R^2} \right) \int_0^R \int_0^{t_{cr}} P(r,t) r \, dr \, dt \tag{9}$$

where $\quad$ R $\quad$ = radius of applied impulse area

r $\quad$ = spatial integration variable

t $\quad$ = time

t_{cr} = critical time

P(r,t,) = spatial-time pressure function symmetric about r = 0.

If a circular slab of radius R and thickness L receives an applied impulse which exceeds I_{cr}, during a critical time t_{cr}, then a breached hole of radius R is assumed to occur. Since I_{cr} is not a function of R or t, a solution may be obtained by a plot of I_{ap} and the t_{cr} line. An example will be discussed later.

2.2.3 Steel Failure Method

This method is based on determining a displacement necessary to cause steel reinforcement failure assuming some deformed reinforcement length. The deformed reinforcement length shown in Figure 2 is assumed to be half the thickness h/2, and the critical strain for failure of reinforcement is assumed to be 0.1.

The equation of motion for the affected slab volume of Figure 2 is written as

$$\rho \pi R^2 h \ddot{w} + 2\pi R h \sigma_{sf} = 2\pi \int_0^R \int_0^t P(r,t) r \, dr \, dt \qquad (10)$$

where

w = displacement

σ_{sf} = ultimate shear stress

σ_s = reinforcement tensile strength.
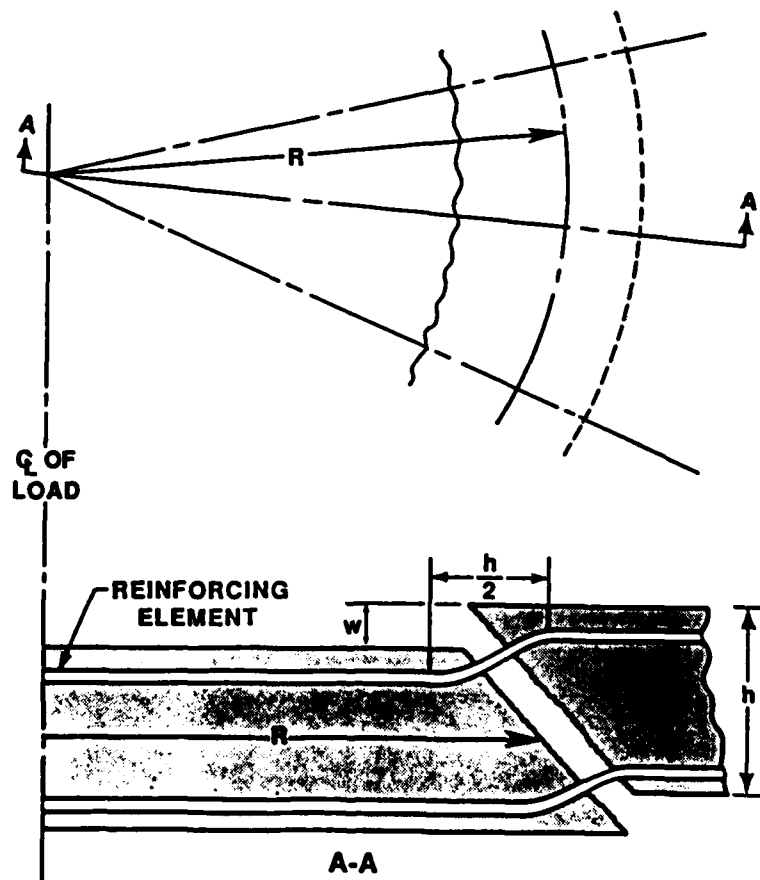
Figure 2. Shear Model for Steel Failure.

8

The solution of Eq. (10) for an assumed pressure distribution (see Figure 4),

$$P(r,t) = P_0(1 - \frac{t}{\tau})(1 - \frac{r}{a}) \exp(-\beta\frac{r}{a}) \qquad (11)$$

where

τ = pulse length of pressure time curve

a = half slab size or extent of pressure loading

β = pressure spatial decay constant

r = radius from center of explosion

is given by

$$\frac{w}{2h} = \frac{P_0 t^2}{2\rho h^2 R^2} (1 - \frac{t}{3\tau}) F(a,R,\beta) - \frac{\sigma_{sf} t^2}{2h\rho R}$$

$$(12)$$

$$F(a,R,\beta) = [\exp(\frac{-\beta R}{a})] (\frac{aR}{\beta} - \frac{a^2}{\beta^2} - \frac{R^2}{\beta} + \frac{2aR}{\beta^2} - \frac{2a^2}{\beta^3}) + \frac{a^2}{\beta^2} + \frac{2a^2}{\beta^3} .$$

From Figure 2 a value of w/2h to give 0.1 reinforcement strain may be determined. The strain in the steel length h/2 for a given displacement w is given as

$$[(\frac{2w}{h})_{sf}]^2 = 0.1 \qquad (13)$$

and the parameter (w/2h) for steel failure is

$$(\frac{w}{2h})_{sf} = 0.079. \qquad (14)$$

A breach radius for steel failure is obtained by plotting w/2h versus radius R for a given time and determining R from the intersection of the $(w/2h)_{sf}$ with t_{cr}. An example is given later.

2.2.4 Concrete Shear Method

For low compressive strength concrete shear failure of the concrete between the reinforcing elements occurs and the concrete is removed leaving the reinforcing elements intact. The failure mode is shown schematically in Figure 3. If a uniform reinforcing spacing of S in each direction is assumed, then a small concrete volume of S^2h, which has four shear faces of area Sh, must be sheared through the thickness to cause concrete shear failure. For a total sheared volume of πhR^2 the total number of small concrete elements is

$$N = \pi hR^2/S^2h = \pi R^2/S^2 \tag{15}$$

and the total through-the-thickness shear area is

$$A_s = 4Sh(\pi R^2/S^2) = 4\pi hR^2/S \tag{16}$$

By using A_s time the concrete shear strength σ_{cf} as a resisting force the equation of motion for concrete shear may be written as

$$\rho\pi R^2 h\ddot{w} + 4\pi hR^2\sigma_{cf}/S = 2\pi \int_0^R \int_0^t P(r,t)rdrdt \tag{17}$$

The solution of Eq. (17) is very similar to Eq. (7), and for the assumed loading of Eq. (6) the solution is

$$\frac{w}{2h} = \frac{P_o t^2}{2\rho h^2 R^2} (1 - \frac{t}{3\tau}) \ F(a,R,\beta) - \frac{\sigma_{cf}t^2}{\rho Sh} \tag{18}$$

where $F(a,R,\beta)$ is defined in Eq. (12).

The assumption for Eq. (18) is that the shear cracks occur simultaneously along the reinforcing element as the load progresses outward from the loading center. A value of $w/2h$ for failure of concrete in shear is not available but the value $w/2h$ is the average compressive through-the-thickness strain for the slab. This would mean that the upper surface of the slab is compressed relative to the lower surface. Both the transverse and axial compressive strain of the current split-Hopkinson bar tests show approximately 0.3-0.5 percent strain at failure; therefore an assumption of 0.3 percent for the average shear strain and $w/2h$ is not unreasonable.
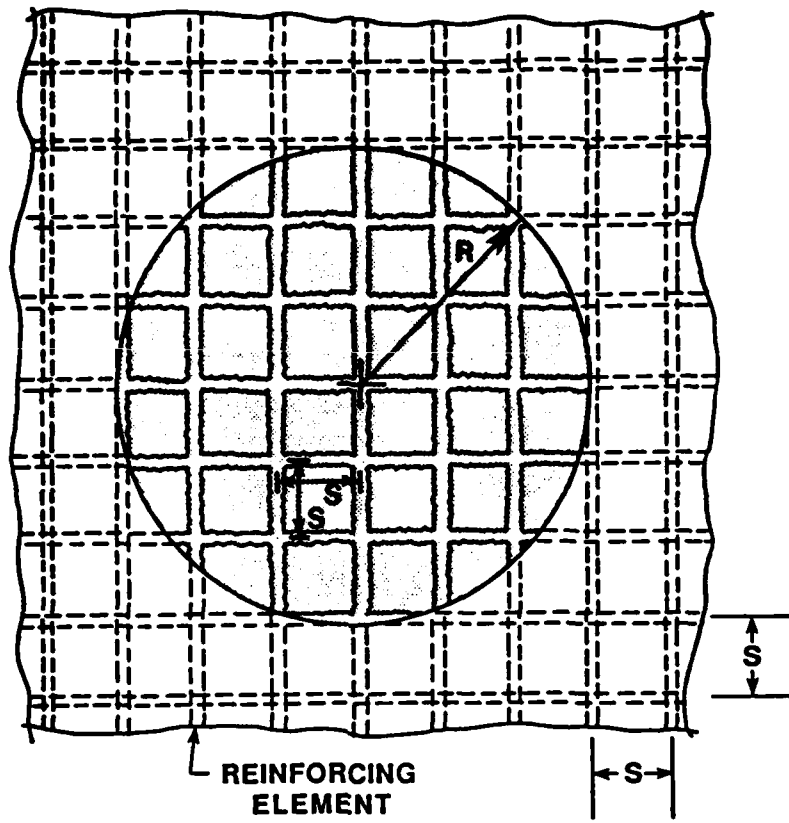
Figure 3. Shear Model for Concrete Failure

$$P_o \left(1 - \frac{t}{\tau}\right)\left(1 - \frac{r}{a}\right) \exp\left(- \beta \frac{r}{a}\right)$$
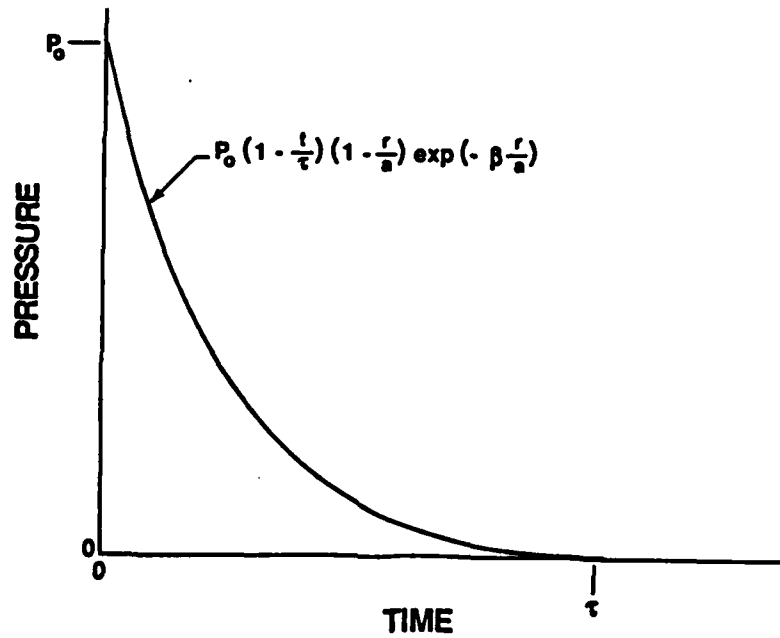
Figure 4. Assumed Pressure Time Function.

11

2.2.5 Example Calculation

A reinforced concrete slab and loading shown in Table 1 was used for comparative calculations of all three methods.

Table 1. SLAB DIMENSIONS AND PROPERTIES FOR SAMPLE CALCULATIONS

Item	Dimensions or Property
o Size L X W X h (Length X Width X Thickness)	12 X 12 X 1 ft 3.66 X 3.66 X .305 m
o Concrete compressive Strength f'_c	5000 psi 34.5 MPa
o Steel yield stress σ_s	50000 psi 345 MPa
o Concrete density ρ_c	4.66 slug/ft^3 1600 kg/m^2
o Steel Density ρ_s	15.2 slug/ft^3 7820 kg/m^3
o Flexural Steel Spacing (both faces)	4 X 4 in 10.2 X 10.2 cm
o Area of Reinforcement ratios (total steel both faces, both directions)	flexural 0.017 (one face 0.0085) shear 0.014
o Loading	8.0 lbs @ 1.0 ft 3.63 kg @ 0.305 m (P_0 = 50,000 psi, a = 72.0, β = -5.0)

For the critical impulse of Eq. (8) the required terms are all given in Table 1. The ultimate shear stress for direct shear is given in Reference 10 as

$$V_u = 0.16 \ f'_c + \mu_c(\sigma_n + q_{sp}\sigma_s) \tag{19}$$

where V_u = direct shear strength (static)

μ_c = coefficient of friction of concrete

f'_c = compressive concrete strength

12

q_{sp} = reinforcement ratio for all reinforcement crossing the shear failure plane

σ_n = normal compressive force across shear plane

σ_s = reinforcement yield strength

For the failure example shown in Figure 2, σ_n = 0 and q_{sp} = q as defined following Eq. (8). Then, with account taken of dynamic increases factors (DIF) for strength due to strain rate effects, the following expression for σ_{sf} is proposed

$$\sigma_{sf} = 0.20 \ f'_c + 1.25 \ q\sigma_s. \tag{20}$$

The coefficient, 0.16, of f'_c in Eq. (19) has been multiplied by a DIF of 1.25 to obtain the coefficient 0.20 in Eq. (20), the friction effect of the second term of Eq. (19) has been neglected by setting μ = 1.0, and steel strength has been multiplied by a DIF of 1.25. Based on low strain rates of 10 or less for initial cracking shown in Table 2, a DIF of 1.25 is considered sufficient for concrete. Strain rate data given in Section III of this report show a reasonably low ratio of dynamic to static strength up to strain rates of 25. Strain rate effects in mild steel at this strain rate are also lower than the value of 1.7 reported for mild steel at a strain rate of 10^3 (Reference 12).

The shear strength σ_{cf} used in Eq. (18) is only the first term of Eq. (20), since in this case only the concrete is being sheared through the thickness. If for some reason the concrete had been extensively cracked by some prior loading the value of σ_{cf} would be reduced. Also, for cracked concrete the term σ_{sf} would be reduced. The effect of cracks on the shear plane was investigated using static loads in Reference 13.

By using Eqs. (12), (14), and (18) with the data of Table 1, plots of w/2h versus radius R for two assumed times were obtained and are shown in Figure 5. The critical time, one quarter of the period of the natural frequency for the slab, was calculated to be approximately one millisecond. A curve for this time and an 0.8 milisecond curve are given in Figure 5. The solid line curves are for the steel failure of Eq. (12), and the broken line curves are for the concrete failure of Eq. (18).

In comparing Eqs. (12) and (14) it is noted that the force term containing the loading P_o, is the same for each equation. The resisting force (term with negative sign) of Eq. (12) is inversely proportional to the radius R, which means that the term decreases with R causing less influence at large R. This then gives the slowly decreasing w/2h curves for steel of Figure 5. However, the resisting force of Eq. (18) is constant for a given reinforcement spacing and has the effect of causing w/2h to decrease faster with increasing R as shown by the almost straight dashed line curves of Figure 5. The effect of the increasing reinforcement spacing is to decrease the resisting force, since the reduced spacing results in less shear surface for failure.

13

TABLE 2. STRAIN RATES IN Z DIRECTION FOR TIMES SHOWN

Time	Integration Locations	8	9	Elements 89	90	170	171
$t_1=.06E-3$ $t_2=.12E-3$	1	.095	-.995	.390	-1.48	1.60	.441
	2	-.077	-2.0	.335	-4.35	5.30	-26.8
	3	.856	-2.0	-.210	-4.35	8.06	-26.8
	4	-1.10	-3.42	-2.05	-8.23	24.3	-185.5
$t_1=.12E-3$ $t_2=.18E-3$	1	.3205	.680	.606	1.736	5.40	48.75
	2	.339	.683	.735	1.816	14.50	-40.00
	3	.586	.683	1.41	1.816	17.06	-40.00
	4	.460	1.116	1.00	3.766	46.67	-308.33
$t_1=.18E-3$ $t_2=.24E-3$	1	-.068	-.473	.856	1.041	7.116	10.03
	2	-.363	.186	2.04	1.23	20.0	-49.00
	3	-.5426	.186	.945	1.23	25.0	-49.00
	4	-.450	2.03	.133	6.15	68.0	-416.66
$t_1=.24E-3$ $t_2=.30E-3$	1	.435	-.783	2.33	.31	13.7	10.03
	2	.556	0.92	3.9	-3.08	42.5	-58.33
	3	-.415	-.92	1.75	-3.08	52.3	-58.33
	4	-15.5	-1.48	-1.93	-.416	153.16	-511.66
$t_1=.30E-3$ $t_2=.36E-3$	1	.875	.176	3.33	23.3	7.0	-2.166
	2	1.725	-.683	4.26	-2.58	22.5	-86.66
	3	.59	-.683	3.916	-2.58	23.2	-86.66
	4	15.5	-2.416	-1.06	-1.35	81.6	-616.6

(continued)

14

TABLE 2. STRAIN RATES IN Z DIRECTION FOR TIMES SHOWN (Continued)

Time	Integration Locations	Elements					
		8	9	89	90	170	171
$t_1 = .6E\text{-}3$	1	1.68	-0.1	2.72	-8.6	-2.5	-81.
$t_2 = .7E\text{-}3$	2	.95	-2.98	.66	-25.3	2.0	-278.
	3	1.23	-3.29	1.05	-33.3	-14.1	-248.
	4	-.68	-7.67	-13.6	-42.9	-39.3	-890.
$t_1 = .7E\text{-}3$	1	1.38	-2.63	-2.24	-26.8	-6.0	-77.
$t_2 = .8E\text{-}3$	2	2.08	-9.6	3.71	-47.6	10.2	-110.
	3	-.05	-8.21	-13.86	-50.9	-50.8	-110.
	4	-4.04	-18.8	-15.40	-117.5	50.4	-600.
$t_1 = .8E\text{-}3$	1	.94	-3.17	.84	-24.8	-15.6	-66.
$t_2 = .9E\text{-}3$	2	.24	-18.6	12.4	-53.0	4.0	40.
	3	-.7	-8.3	-11.2	-49.0	-77.6	30.
	4	-8.01	-39.2	0.9	-187.0	99.9	-210.
$t_1 = .9E\text{-}3$	1	1.65	4.62	1.32	-12.5	-12.4	-61.
$t_2 = 1.0E\text{-}3$	2	1.84	-10.3	5.9	-52.0	23.2	140.
	3	5.77	-2.7	0.0	-46.0	-100.0	130.
	4	4.40	-52.7	3.9	-202.0	128.0	90.

15

The results of Figure 5 show that, for a time of 1.0×10^{-3} sec, steel failure and concrete failure will occur at about the same radius of 18 inches. At the 0.8×10^{-3} second time the calculations show that steel failure may occur prior to concrete failure at a radius of 10 inches but steel failure may not occur at all for times much less than 0.8 sec.

In comparison the critical impulse results of Eqs. (3) and (4) for the same slab of Table 1 are shown in Figure 6. The critical impulse method predicts a larger failure radius, 22 inches, than either of the other two methods presented in this study.
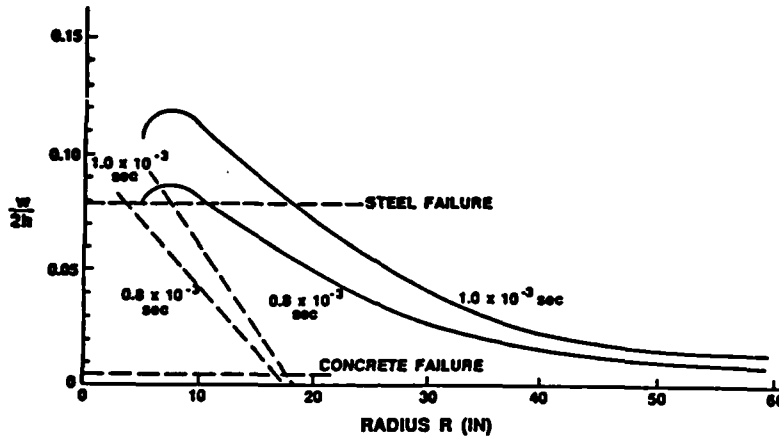
Figure 5. Normalized Displacement Versus
Radius for Shear Models.
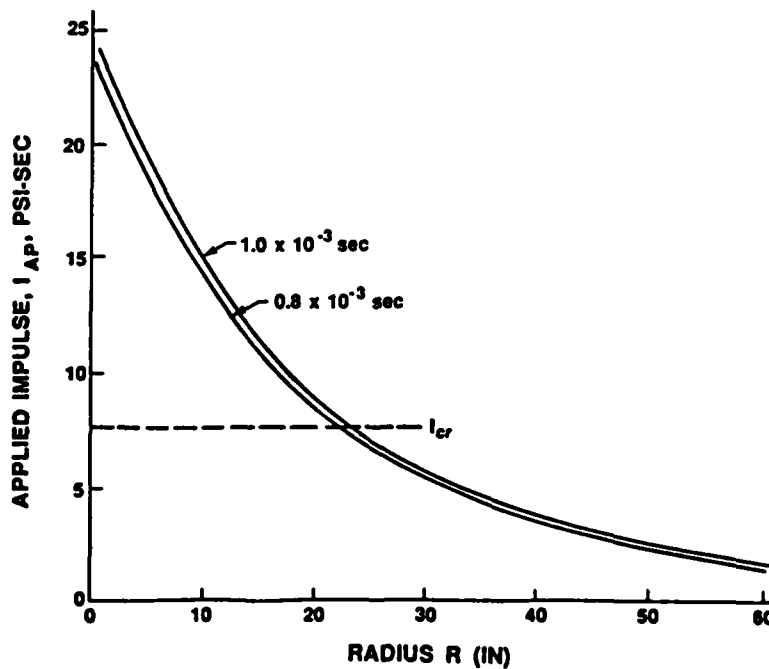
Figure 6. Applied Impulse for Assumed Pressure
Time Function Versus Radius.

16

2.3 Finite Element Calculations

2.3.1 Introduction

The same slab and loading as were used in the calculations of Section 2.2 were also used in the finite element code (FEM) NONSAP-C (Reference 14). For this calculation the loading is based on the model presented in Section 2.1. The original finite element code was modified to accept this loading model and the strain rate effects equation for concrete given in Reference 1. The strain rate effects for concrete were incorporated using a strain rate factor (SRF) applied to the compressive strength f_c'. This strain rate factor is given as

$$SRF = 1 + \frac{B}{A} (\dot{\varepsilon}_1 / \dot{\varepsilon}_0), \tag{21}$$

where $\dot{\varepsilon}_1$ is the current strain rate of the previous time step, B and A are determined experimentally as in Reference 1 and 2. The reference strain rate $\dot{\varepsilon}_0$ was chosen to be 10^{-3}/sec. The current strain rate for the FEM run was determined by the difference in strain of the two previous time steps divided by the difference in the time steps. The strain rate sensitivity of the reinforcing steel is given by

$$\frac{\sigma_{dy} - \sigma_{sy}}{\sigma_{sy}} = \begin{cases} 0.167 \log_{10}(\dot{\varepsilon}/\dot{\varepsilon}_0), & \dot{\varepsilon} > 10^{-4} \\ 0 & , & \dot{\varepsilon} \leq 10^{-4} \end{cases} \tag{22}$$

where σ_{dy} is the dynamic yield strength, σ_{sy} is the static yield strength and $\dot{\varepsilon}_0$ is chosen to be 10^{-4}/sec.

2.3.2 Results

Results of the slab configuration of Table 1 are given in terms of strain rate and crack density. The results of strain rate for strains in a direction normal to the slab are given in Figure 7.

Concrete cracking in the FEM analysis progresses outward from the center of the slab with increasing time. Figure 8 shows this progression on the elements along the center line of the slab. The locations of the elements are shown in Figure 7.

The concrete cracking progresses outward in Figure 8 with single cracks denoted by positive sloping lines, followed by 2 cracks denoted by the negative sloping lines, and 3 cracks denoted by horizontal lines. In the FEM model each element has 8 integration points, each of which may indicate cracking. In Figure 8 each element is divided in half, each containing 4 integration points. If two of the four integration points have 1, 2, or 3 cracks then the half element is marked in that manner.
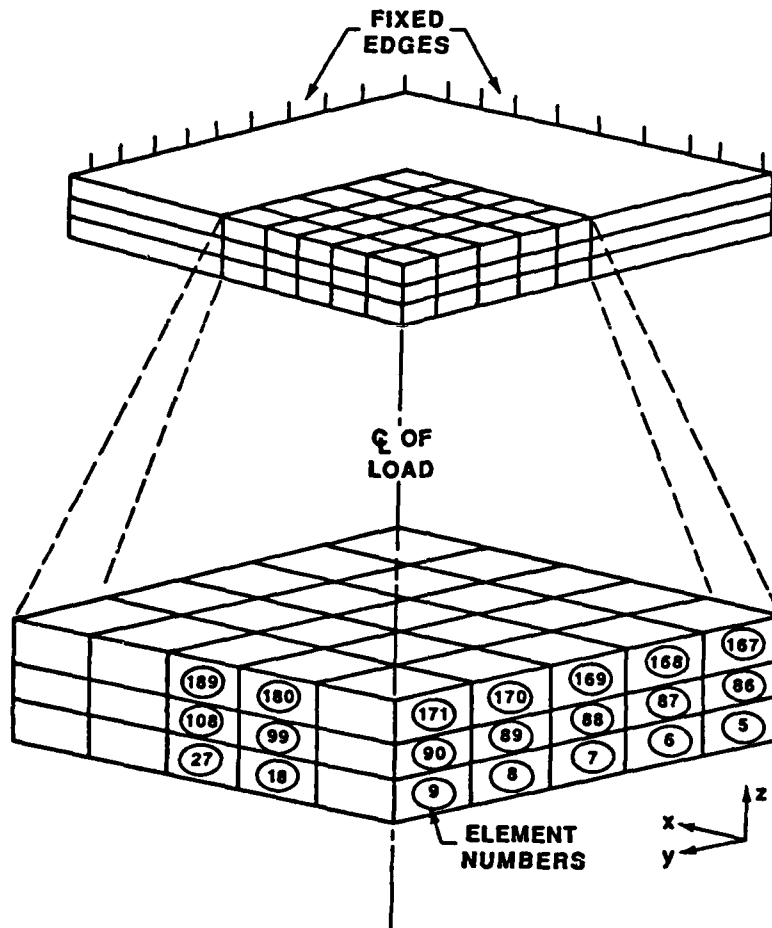
Figure 7. Element Identification for Crack Density
Display of Figure 8.

As evidenced by Figure 8 the lower or bottom elements appear to form cracks first, which lends some credence to the assumption of the sloping damaged zone of Figure 2. At $t = 1.0 \times 10^{-3}$ sec the outer edge of the crack pattern of Figure 8 appears at approximately 40 inches (5 elements from the center of the load), whereas the center of the 3-crack region is at about 24 inches. From Figure 5 the edge of steel failure region is approximately 18 inches at this time.

18

℄
OF LOAD

|←———— 72" ————→|

8"

171	170	169	168	167	166	165	164	163	4"
90	89	88	87	86	85	84	83	82	
9	8	7	6	5	4	3	2	1	

ELEMENT NOS.
SEE FIG. 7

t = 0.6 x 10⁻³ sec

t = 0.2 x 10⁻³ sec

t = 0.7 x 10⁻³ sec

t = 0.8 x 10⁻³ sec

t = 0.4 x 10⁻³ sec
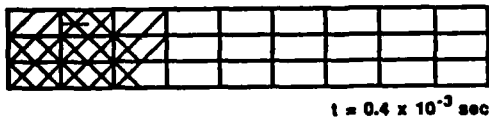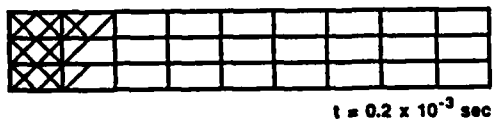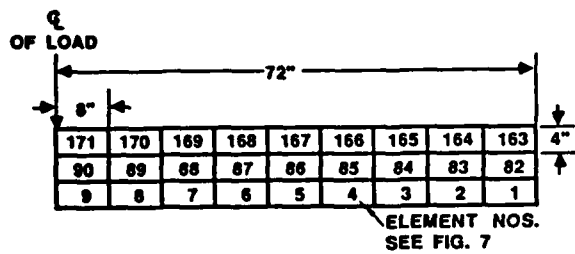
| SYMBOL | ▱ | ▨ | ▨ |
| NO. OF CRACKS | 1 | 2 | 3 |

t = 0.9 x 10⁻³ sec

t = 1.0 x 10⁻³ sec
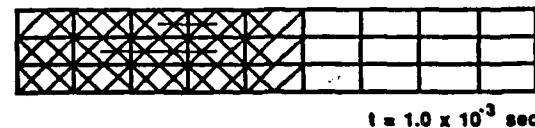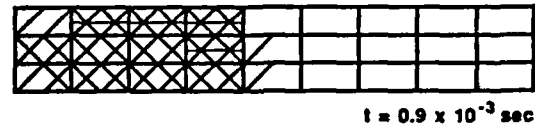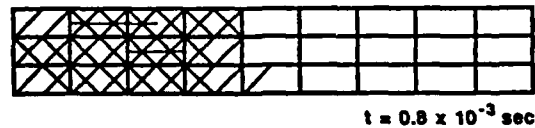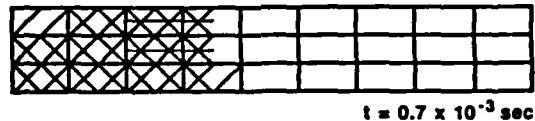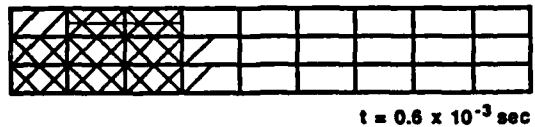
Figure 8. Crack Density for Center Line Elements
of Slab Shown in Figure 7 and Used in
the Finite-Element Analysis.

By using the condition of Eq. (14) the displacement at a radius of
18 inches is calculated to be 1.9 inches. The maximum displacement predicted
by the FEM analysis is 4.0 inches at the center node directly underneath the
load but is less than 0.1 inches at a point halfway out from the center of the
load.

Summary and Conclusions of Task I are presented in Section 4.1.

19

SECTION III

TASK II: DYNAMIC STRENGTH OF CONCRETE

3.1 Introduction

Finite-element codes for structural response of reinforced concrete use as a parameter the unconfined compressive strength of the concrete, f_c', which is sometimes increased by an arbitrary factor for dynamic loading. The objective of this research was to determine the rate dependence of f_c' at rates of interest for the structural response (mainly below 100/sec) and eventually to model the rate-dependent constitutive behavior. Results of tests on mortar with a small Kolsky bar system and of a newly built larger system on concrete with a maximum aggregate size 1/2 inch have been obtained with strain rates at the maximum stress from 50 to 800/sec for mortar and from 5 to 120/sec for concrete. An apparent rate dependence up to almost twice the static strength was observed for both. The mortar shows an apparent linear dependence, while the high-strength concrete shows an approximately logarithmic dependence on the strain rate at the maximum stress over the dynamic range observed, although the fitted logarithmic dependence does not extend down to quasistatic rates. Some questions about specimen size effects and about how much of the apparent strain-rate effect is really a lateral inertia confinement effect are as yet unresolved. Continuing research is focused on observation of the lateral motion to assess lateral inertia effects in unconfined specimens and on passive confinement by metal jackets.

The results on mortar were described in the First Annual Report (Reference 1) and in a published paper (Reference 15). A brief summary is given in Section 3.4.1 of this report. These results on mortar were obtained with an existing Kolsky apparatus at the University of Florida, and the experience gained was used to guide the design of a new larger Kolsky apparatus, which was fabricated during the first year of the contract.

The Kolsky apparatus or Split Hopkinson's Pressure Bar (SHPB) system consists of two long strain-gaged pressure bars with a short specimen sandwiched between them. Analysis of the observed longitudinal elastic stress wave propagation in the two pressure bars furnishes information about both the force and displacement versus time at each specimen interface. The specimen is supposed to be so short that waves propagate back and forth between its two interfaces and achieve an approximately uniform state of stress and deformation along the specimen length, except during the initial rapid rise of the stress. Various versions of the SHPB system have been used in recent years for testing rock, mortar and fine-grained concrete. Most of the existing systems have a maximum specimen diameter of 25 mm. In structures of interest, concrete aggregate sizes up to 0.5 inch (12.5 mm) or even larger may be used. For such concrete, a larger specimen must be used in order to obtain representative properties of the material. The new system with 75-mm diameter pressure bars was developed for this reason.

The larger specimen and larger-diameter pressure bars, however, introduce two problems. For longer specimens the desired degree of uniformity along the length is not achieved. For example, with specimens 2.6 inches long the possible error in stress measurement at an average strain of 0.004 was estimated to vary from about 2 percent at low impact speeds to 5 percent at moderate speeds and 18 percent at the highest speeds in the test series. The

error was smaller at the maximum stress (1 to 5 percent) but larger at smaller strains where the stress was changing rapidly--as much as 40 to 50 percent possible error at a strain of 0.002. Maximum stresses are still reasonably well measured, but the stress-strain curve determination involves some uncertainty about what stress to associate with the average strain at each instant. The larger diameter also leads to more noticeable Pochhammer-Chree radial oscillations in the incident pressure bar, which interfere with the interpretation of the longitudinal strain measurement in the incident pressure bar and hence interfere with the force and displacement recording at the specimen's incident bar interface.

Despite these problems, the SHPB system appears to be the best available system for determining dynamic compressive properties in the moderately high deformation rate range. For 3-inch-long plain concrete specimens, the system has performed tests at strain rates ranging from 5 to 120 sec^{-1} at failure.

The new system was described in the Second Annual Report (Reference 2) and in two publications (References 16 and 17) and will be briefly described in Section 3.3 of this report. Results of unconfined dynamic compression tests on four kinds of high-strength concrete were also given in these three references and will be reviewed in Section 3.4.2, along with some results on a new high-strength concrete prepared at SRI International.

During the last year unconfined tests have been performed on SIFCON, a slurry infiltrated fiber concrete with steel fiber reinforcements, with a dynamic compressive stress-strain curve similar to that of a ductile metal, as described in Section 3.4.3. The fiber reinforcement in effect confined the lateral expansion and prevented the typical brittle failure exhibited by plain concrete in unconfined tests.

In Section 3.5 exploratory tests of three different kinds are reported. These have led to some interesting tentative conclusions--tentative because they are based on a limited number of tests and need further verification. Exploratory axial compressive tests on mortar and plain concrete confined by metal jackets to restrict the lateral expansion were performed during the last year, as will be described in Section 3.5.1. These tests also gave a stress-strain curve similar to that of a ductile metal. The procedure needs further refinement, but the preliminary results suggest that with further optimization of the technique important information can be obtained about the dynamic behavior under confinement.

Further analysis of the digitally recorded data of the unconfined tests has also revealed some important information.

Some observed delay-time phenomena are reported is Section 3.5.2. At low speeds of striker-bar impact there appears to be a delay time before the initiation of microcracking. At somewhat higher impact speeds a further delay time was observed between the onset of microcracking and the time when the microcrack development leads to general failure and apparent strain softening. These two kinds of delay-time effects may be the source of much of the rate dependence in the lower-speed tests where lateral intertia confinement is not significant.

Radial inertia effects, which provide a confinement of the interior of the specimen and result in enhanced axial strength that is not really a

21

material rate sensitivity will be mentioned in the background Section 3.2. In Section 3.5.3, some estimates are reported of the radial acceleration and lateral inertia in the SHPB tests. It appears that radial inertia effects are important only at the higher testing speeds.

Summary and conclusions are given in Section IV.

3.2 Background

A detailed literature survey was presented in Reference 17. A condensed version is given here.

Early work on rate effects in concrete was reviewed in a 1956 ASTM symposium [18]. At stress loading rates from 1 to 1000 psi per second in testing machines, compressive strength was reported to be a logarithmic function of the loading rate with recorded strength increases up to 109% of the strength reported at "standard rates" (20 to 50 psi per sec). By using cushioned impact tests Watstein [19] obtained strengths 185% of the standard.

The compressive SHPB, introduced by Kolsky [20] is widely used for determining material properties in the strain-rate range from about 10^2 to 10^4 sec^{-1}. See, e.g., Lindholm [21] and Nicholas [22]. Geotechnical materials and concrete have been tested with the SHPB. Bhargava and Rehnstrom [23] found unconfined dynamic compressive strengths of 1.46 to 1.67 times the static strength in plain concrete and fiber-reinforced and polymer-modified concrete. Their failure strengths were identified as the maximum amplitude of short-pulse stresses that could be transmitted.

At the University of Florida, Tang et al. [15], tested 28-day mortar specimens in a 3/4-inch diameter SHPB and found a linear dependence of maximum stress on the strain rate at the maximum stress at rates up to 800 sec^{-1}. Few other applications of SHPB technology to concrete have been made. Kormeling et al. [24], adapted it for dynamic tensile tests. They reported dynamic tensile strengths of more than twice the static value at strain rates of approximately 0.75 sec^{-1}. Malvern et al. [16,17] have reported high-strength concrete tested with the SHPB system to be described in this report. Suaris and Shah [25] and Shah [26] have recently surveyed properties of materials subject to impact and rate effects in fiber-reinforced concrete.

Radial inertia effects in geotechnical materials, which may be mistaken for strain-rate effects, were discussed by Glenn and Janach [27] and by Young and Powell [28]. In their tests it appears that failure occurred during the first passage of the stress wave through the specimen. In the SHPB tests reported here failure occurs only after many wave reflections back and forth between the specimen interfaces. Bertholf and Karnes [29] made a two-dimensional numerical analysis of the SHPB system and concluded that with lubricated interfaces the one-dimensional elastic-plastic analysis was reasonable if limitations are imposed on strain rate and rise time in the input pulse and specimen length to diameter ratio is about 0.5.

3.3 Brief Description of New Equipment and Procedures

The experimental facility consists of a gas gun, which propels a projectile that acts as a striker bar to impact axially the incident pressure bar, which transmits the loading pulse to the specimen sandwiched between the

incident pressure bar and the transmitter pressure bar. The gas gun was fabricated by Terra-Tek Systems, Inc. As currently configured, it fires a 30-inch-long, 3-inch-diameter, 61.28-lb steel striker bar to impact at speeds V_0 up to 50 ft/sec with firing chamber pressures up to 500 psi. Higher speeds are possible with a lighter impactor or a higher firing pressure. The propellant gas is furnished by a nitrogen bottle (2000 psi maximum). The firing chamber was proof tested to 3000 psi, but, as currently configured, a safety valve in the control system limits the firing pressure to 750 psi to avoid damaging the pressure gauge. The 3-inch-diameter striker bar is guided in the 3.125-inch-diameter gun barrel by two Teflon bushings attached to the striker bar, which act as pressure seals until the aft bushing passes pressure-relief vent holes in the barrel.

The 120-inch-long incident and transmitter pressure bars are mounted in pillow blocks supported by a steel frame structure. The whole system including gas gun, pressure bars and a shock absorber with 6.5-inch stroke at the far end is almost 30 feet long. The projectile nose protrudes about 1.5 inches outside the muzzle when it strikes the incident pressure bar and may travel up to 8 inches farther before the pressure bars are stopped by the crushing specimen and the shock absorber. A sleeve is mounted on the gun muzzle to protect nearby personnel; the sleeve also supports the forward Teflon bushing of the projectile after a firing.

A full strain-gage bridge is permanently mounted on each pressure bar, 60 inches from the specimen interface. Each bridge consists of two double element strain gages (Micro-Measurements Type WA-06-250TB-350) mounted on opposite sides of the bar. The gage elements are oriented to coincide with the longitudinal and transverse directions of the bar. The amplified signals are recorded by a transient recorder consisting of a four-channel Nicolet 4094 digital storage oscilloscope. The recorded signals are displayed by the oscilloscope and also stored on floppy diskettes for subsequent analysis.

Figure 9 is a schematic of the pressure bar arrangement, with a Lagrange diagram above it illustrating the elastic wave propagation in the pressure bars. Figure 10 shows an example of the axial strain signals versus time, recorded by a Hewlett Packard 7470A digital plotter from the stored signals in the digital oscilloscope. Compressive strain is plotted upward. After the passage of the first incident pulse, of nominal length 300 microsec (from the beginning of the rise to the beginning of the fall), there is a dwell time before the arrival of the reflected pulse from the specimen, which is recorded at the same gage station as the incident pulse. Another channel shows the pulse transmitted through the concrete specimen into the transmitter bar. Because the two gage stations are equidistant from the specimen, the transmitted pulse arrives at the transmitter-bar gage station at approximately the same time as the reflected pulse arrives back at the incident-bar station, delayed only by the transit time of the leading edge of the pulse through the specimen (about 16-18 microsec for a 2.6-inch-long concrete specimen). Also shown are records from two strain gages mounted on the specimen midway between its ends, one measuring axial surface strain ϵ_z and one measuring transverse (hoop) strain ϵ_θ. The drop in ϵ_z at 424 microsec corresponds to a failure in the specimen, but the gage continued to function. At 466 microsec the ϵ_θ gage failed.
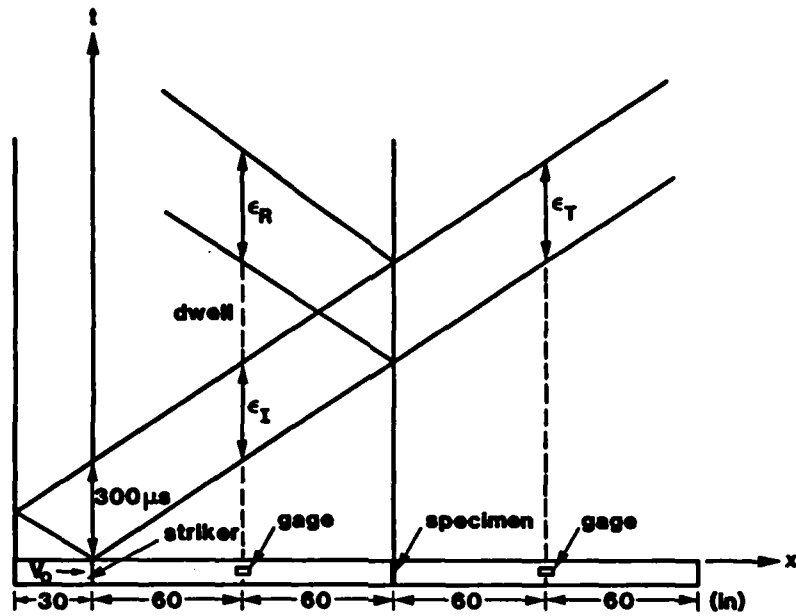
Figure 9.   Schematic of Bars and Lagrange Diagram.
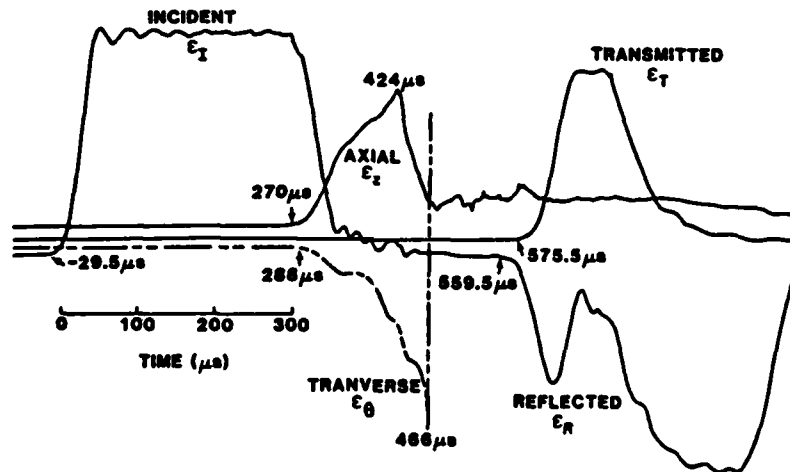
Figure 10.   Strain Pulses in Pressure Bars and Axial
and Transverse Specimen Surface Strains.

40 (KSI)   STRESS   (MPa)

σ_I

σ_2

σ_1

σ_R

30 — 200

20 —

— 100

10 —

0   80   160   240   320

TIME (μs)
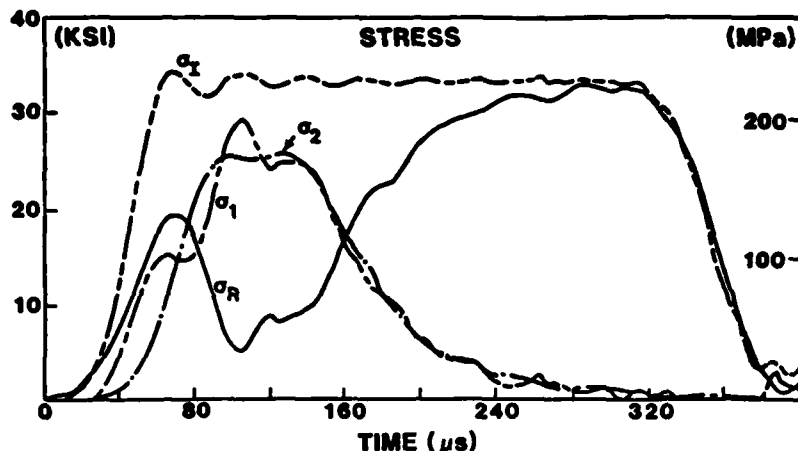
Figure 11. Pressure Bar Interface Stresses (time-shifted)
From Record of Figure 10.

For purposes of analysis, the digitally recorded pulses are time shifted,
so that time zero coincides with the initial arrival at the specimen inter-
face. Figures 11 to 14 are for the same 2.6-inch-long specimen whose raw data
was illustrated in Figure 10. Figure 15 is for another specimen at a higher
impact speed. Figure 16 is for a 1.32-inch-long specimen of the same material
(maximum aggregate size 3/8 inch). In Figure 11, the pressure-bar strain
pulses have been converted to stress pulses by multiplying by the elastic
modulus of the steel. The reflected pulse σ_R is shown inverted, and all
pulses have been shown as stresses in the pressure bars at the interfaces with
the specimen. The total stress σ_1 at the incident interface, which is the
algebraic sum of the incident σ_I and reflected σ_R is also plotted. The σ_1
record rises very slowly at first, and then rises smoothly until about 14 KSI,
where something resembling a small step occurs. This may be associated with
three-dimensional effects at the the end of the pressure bar interacting with
the axial stress waves propagating back and forth in the specimen. Note that
the step coincides approximately with the first dip in the Pochhammer-Chree
oscillations in the incident pulse. Correction for the dispersion in the
pressure bar may eliminate some of the irregularities in the σ_1 record [30].
Since the specimen cross section is the same as that of the pressure bar, in
the one-dimensional analysis the stress σ_1 is considered to be the specimen
stress at the first interface, and the specimen stress σ_2 at the second inter-
face is equal to the transmitted stress σ_T. For this 2.6-inch-long specimen,
σ_1 and σ_2 do not become equal before the maximum stress.

Figure 12 shows the stress σ_2, the average stress $\overline{\sigma} = \frac{1}{2} (\sigma_1 + \sigma_2)$, the
average strain rate $\dot{\varepsilon}$ deduced from the difference in the two interface velo-
cities as calculated from the one-dimensional elastic bar-wave analyses in the
pressure bars, without any correction for dispersion, and the average strain
ε obtained by numerical integration of the average strain rate, all plotted
versus the time measured from the first pulse arrival at the first interface.
Note that in Figure 12 the strain rate is approximately constant in the
vicinity of the maximum stresses, except for some oscillations introduced by
the oscillations in the incident pulse. Figure 13 shows $\overline{\sigma}$ and σ_2 versus the
average strain ε.

25
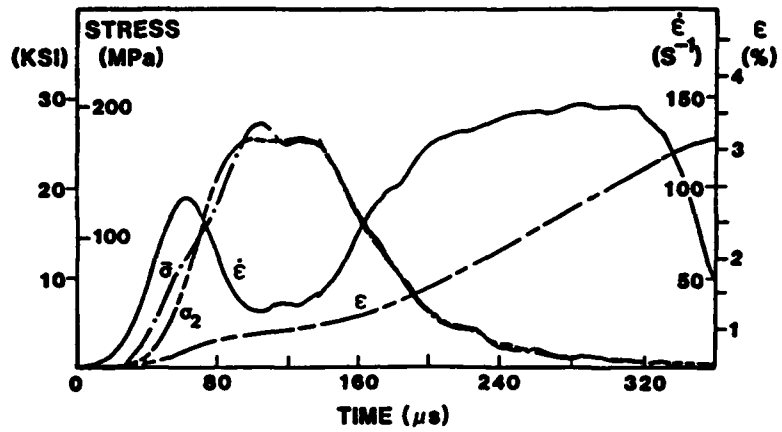
Figure 12. Transmitted and Average Stresses, Strain Rate and Strain Versus Time.
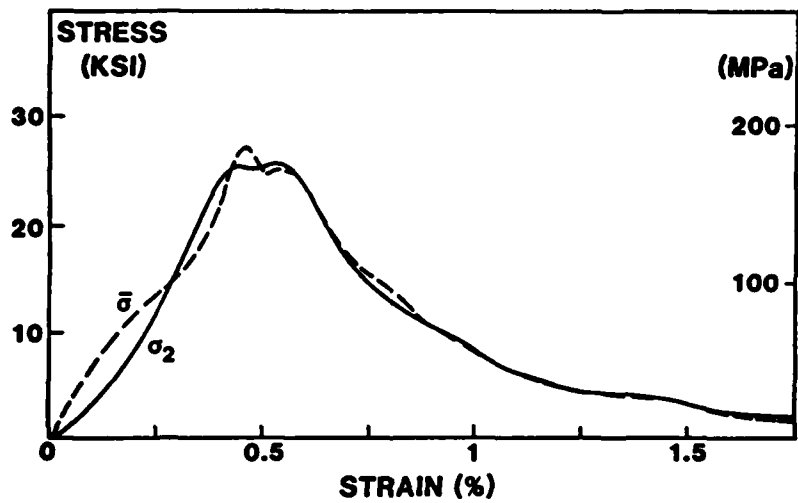
Figure 13. Stress-Strain Curves.

26
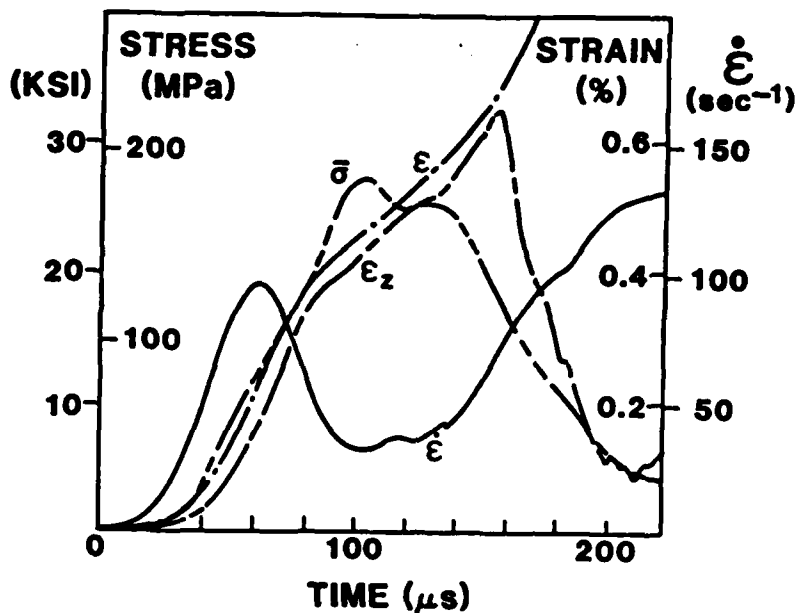
Figure 14. Specimen Gage ε_z Compared with Average Strain $\bar{\varepsilon}$.
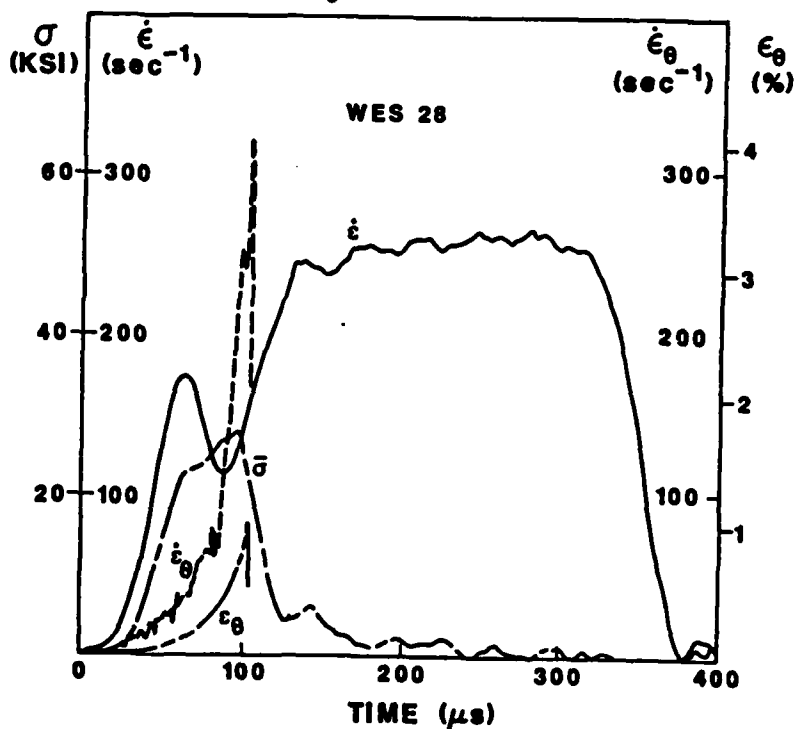

Figure 15. Transverse Strain Rate Indicates That Significant Lateral Acceleration Occurs Only After Stress Is Well Above the Static Ultimate Strength.

27
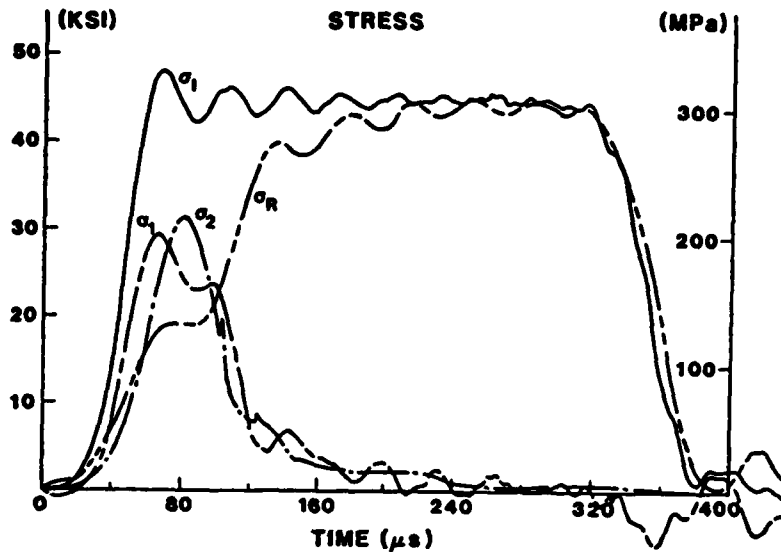
Figure 16. Pressure Bar Interface Stresses
for a 1.32-inch-long Specimen.

Figure 14 compares the average strain ε to the specimen-gage strain ε_z, and also repeats the average stress and strain-rate curves. The drop in ε_z, which is attributed to a fracture in the specimen, occurs well after the maximum stress.

Figure 15 shows the transverse strain from the surface strain gage and also shows the transverse strain rate $|\dot{\varepsilon}_\theta|$ obtained by numerical differentiation of a smoothed ε_θ record. Its rapid rise from about 65 microsec corresponds to a radially outward acceleration of the surface, which could cause lateral inertia confinement of the interior of the specimen and may account for part of the more rapid rise in stress after about 75 microsec. The static ultimate strength of these specimens is not more than 17 KSI and σ_1, σ_2 and $\bar{\sigma}$ have all far exceeded this value well before the 65 microsec time at which radial inertia effects appear. In these tests at moderate impact speeds, failure occurs well after a single transit time of the stress wave through the specimen (about 16-18 microsec).

Figure 16 shows the time-shifted pulses represented as interface stresses in the 1.32-inch-long specimen. There is no step in the rising portion of σ_1, but a dip appears later in that curve, approximately coinciding with the first dip in the Pochhammer-Chree oscillation on the incident pulse. This suggests that the step or dip in the first interface stress record is an artifact of the calculation procedure. The first and second interface stresses, as plotted in Figure 16 still do not become equal before the maximum stress is reached, even for this shorter specimen.

3.4 Main Results of Unconfined Compressive Tests

3.4.1 Mortar tests

Figure 17 summarizes results for an extensive series of tests on mortar specimens with the 3/4-inch diameter SHPB system [15]. Each plotted point represents the average for 4 to 7 tests at the same impact speed for specimens

from two batches of the mortar. The dynamic results in this case are well fitted by a linear plot up to a strain rate of 800 sec^{-1}. The slope of the fitted line for four batches of mortar is 6.61 psi-sec (45.2 x 10^{-3} MPa·s).
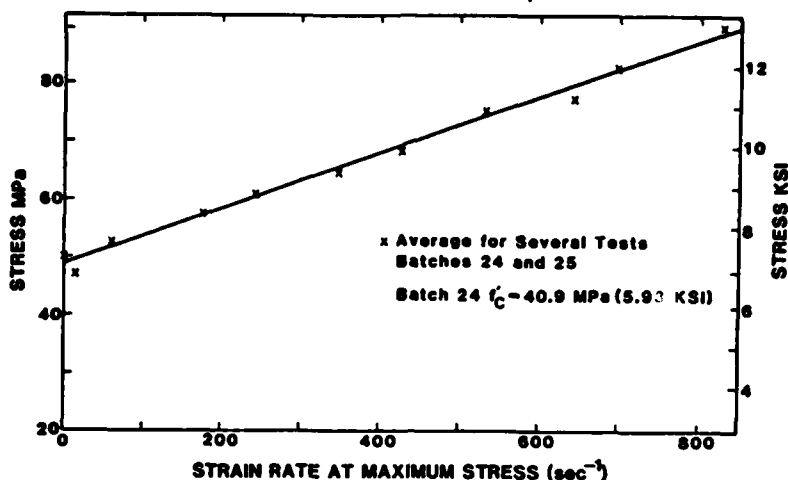

Figure 17.   Maximum Stress Versus Strain Rate at Maximum
Stress in Dynamic Compression Tests of Mortar.

3.4.2   High-Strength Concrete Tests

Four types of high-strength concrete have been tested and results published [16,17]. All four concretes have water/cement ratio around 0.24 to 0.27 and are specified as 14 KSI concrete, based on standard static unconfined compression tests. They differ mainly in the type of coarse aggregate used. Three of them were prepared, cured and cored from blocks by Terra Tek, Inc. of Salt Lake City. The three aggregates they used (maximum size 1/2-inch dia.) are designated as Andesite, Seattle gravel, and a lightweight aggregate called Solite. The fourth material with a manufactured limestone aggregate (maximum size 3/8 inch) was prepared at the U. S. Army Waterways Experiment Station (WES), cast in PVC pipe molds of 3-inch diameter and cut to length after cure. They were further machined and ground at the University of Florida to ensure end face parallelism within 0.0005 inch. Many additional tests have now been made on the WES concrete [mix details below] and most of the results in this report are for it.

Mix for Waterways Experiment Station Concrete

[1 cubic yard]   Slump 8.5 inches

Water/Cement Ratio (based on total cementitious material)	0.27
Type I Portland Cement	850 lb
Silica Fume	150 lb
Fine Aggregate (Manufactured Limestone from Vulcan Materials, Calera, Ala.)	1860 lb
Coarse Aggregate (Manufactured Limestone maximum size 3/8 inch)	1008 lb
Water	270 lb
High Range Water Reducing Add Mixture	20 lb

DAXAD-19-2% by weight of cementitious material (superplasticizer). Prepared by Concrete Technology Division, WES

Figure 18 shows a selection of six dynamic stress-strain curves for this material obtained with different striker-bar impact speeds. Each curve is labeled by the strain rate at the maximum stress, except for the one at the lowest speed impact where the specimen appeared to be undamaged after the test. Note that the zero strain points for the different curves are offset to prevent them from overlapping.

Figure 19 shows a plot of maximum stress versus the strain rate at the maximum stress for 22 of the WES limestone-aggregate concrete specimens. One specimen (not shown) supported a dynamic stress of 19.2 KSI without fracture. The two highest rate tests are plotted twice, once with the average stress at the two interfaces and once with the second-interface stress (open circles). The suitability of the choice of abscissa in this plot is open to question, but it seems to correlate the data. The plot shows dynamic strengths for the WES concrete varying from 19.6 KSI at a strain rate of 5.25/sec up to more than 30 KSI at 120/sec. In preliminary tests [16], the Andesite specimens had a static strength of 16.1 KSI and dynamic strengths varying from 20.4 KSI at 12/sec up to 28.0 KSI at 77/sec. The Seattle gravel dynamic strengths varied from about 12 KSI at 10/sec to 18 KSI at 118/sec. The highest failure stress recorded for Solite was 19.6 KSI.
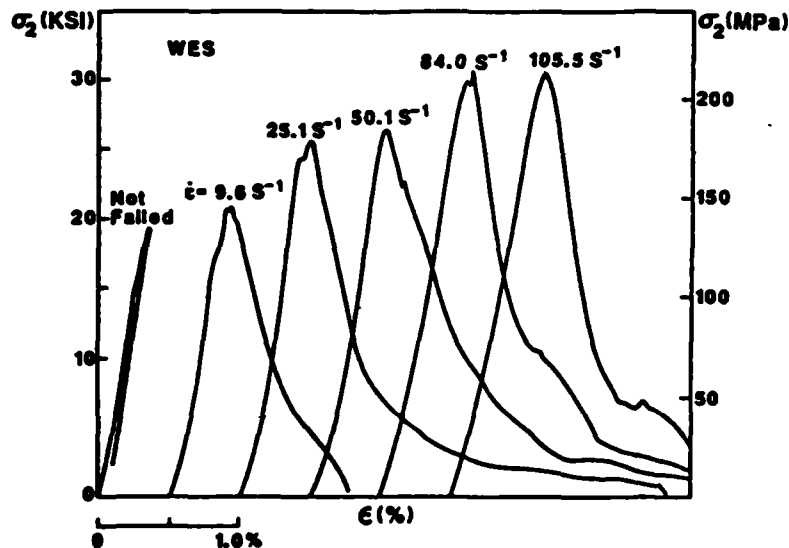
Figure 18. Dynamic Stress-Strain Curves for
WES Limestone-Aggregate Concrete.

The dynamic test points on the curve of Figure 19 are well fitted by a semilog curve of the form

$$\sigma = A + B \ln (\dot{\varepsilon}/\dot{\varepsilon}_0)$$

with   (23)

$$\dot{\varepsilon}_0 = 1 \text{ sec}^{-1}, \quad A = 101 \text{ MPa (14.6 KSI)}, \quad B = 23.4 \text{ MPa (3.39 KSI)}$$

30

over the dynamic range of a little over one decade in strain rates, but this logarithmic representation will not extend to the quasistatic tests at strain rates of order 10^{-3} or 10^{-4} sec^{-1}.
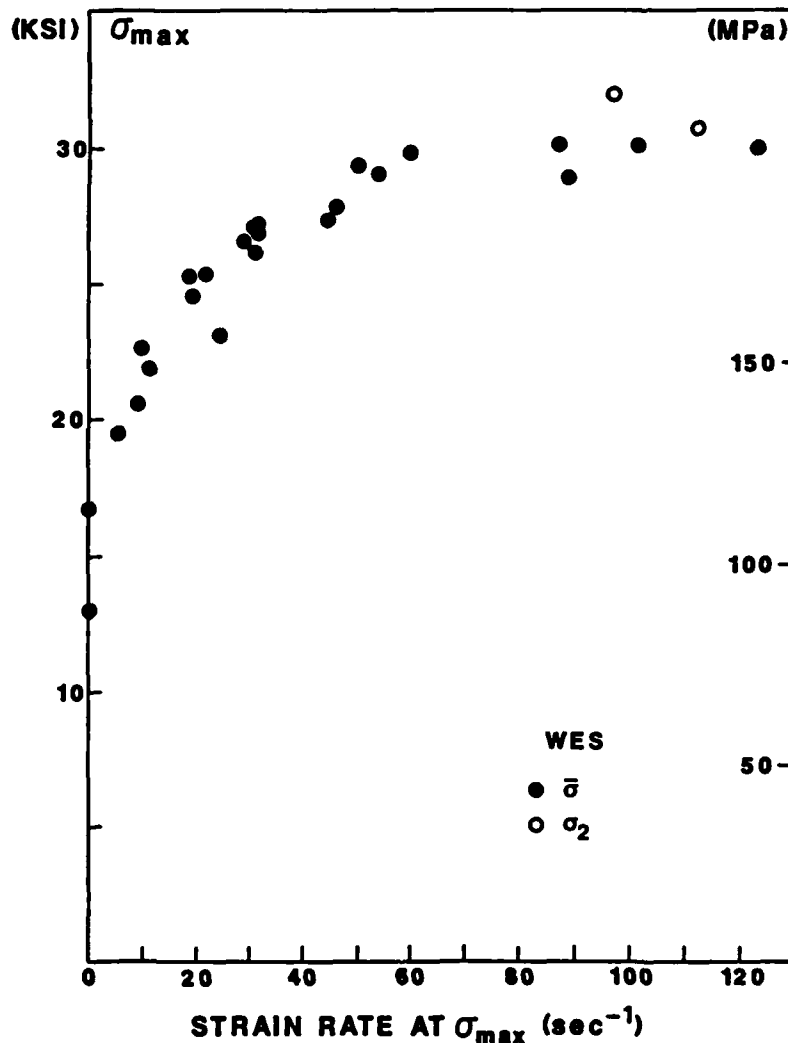
Figure 19. Maximum Stress Versus Strain Rate at the Maximum Stress for 22 WES Specimens.

During the final year of the contract tests were performed on 32 specimens of a high-strength concrete prepared at SRI International and furnished by James K. Gran of the Shock Physics and Geophysics Department of the Poulter Laboratory of SRI International. Details of the concrte mix were not given, but the dynamic performance was similar to that of the WES concrete. Specimens were 3 inches in diameter; 27 of them were 1.5 inches long and 5 were 3 inches long.

The results of the 32 tests are summarized in Figure 20, a plot of the maximum stress attained versus the strain rate at the maximum stress. The stress plotted is the second interface stress σ_2, that is the stress at the interface

between the specimen and the transmitter bar, since the stress at the first
interface (with the incident pressure bar) is not considered to be as reliable as
the second interface stress. The two points at the far left, marked with open
circles, are for the two lowest-speed impacts, where there was no apparent
external evidence of failure. The solid circles are for the 25 short specimens,
where the maximum stress marks the onset of strain softening. Points marked with
an X are for the longer (nominally 3 inch) specimens. No size effect is
apparent.

Figure 20 also has added for comparison 7 points marked by solid squares.
These are previously obtained results on limestone aggregate specimens of
length 1.26 inch to 1.36 inch, prepared at Waterways Experiment Station (WES).
The two materials seem to be essentially equivalent in these tests. Previous-
ly noted size effects in the WES concrete may be partly attributable to the
fact that the average of the two interface stresses was used, and there were
some anomalies in the first interface stress measurement. In the comparison
of Figure 20, the second interface stress was reported for both materials.

The data for the 25 SRI 1.5-inch-long specimens were fitted by a semi-
logarithmic expression of the following form.

$$\text{Max} \quad \sigma_2 = A + B \ln (\dot{\varepsilon}/\dot{\varepsilon}_0)$$

with   (24)

$$\dot{\varepsilon}_0 = 1 \text{ sec}^{-1} \qquad A = 91.3 \text{ MPa} \quad (13.24 \text{ KSI}) \qquad B = 23.3 \text{ MPa} \quad (3.38 \text{ KSI}),$$

arbitrarily referred to a reference strain rate of 1 sec^{-1}. The solid curve
in Figure 20 is a plot of this fitted expression for dynamic data only.
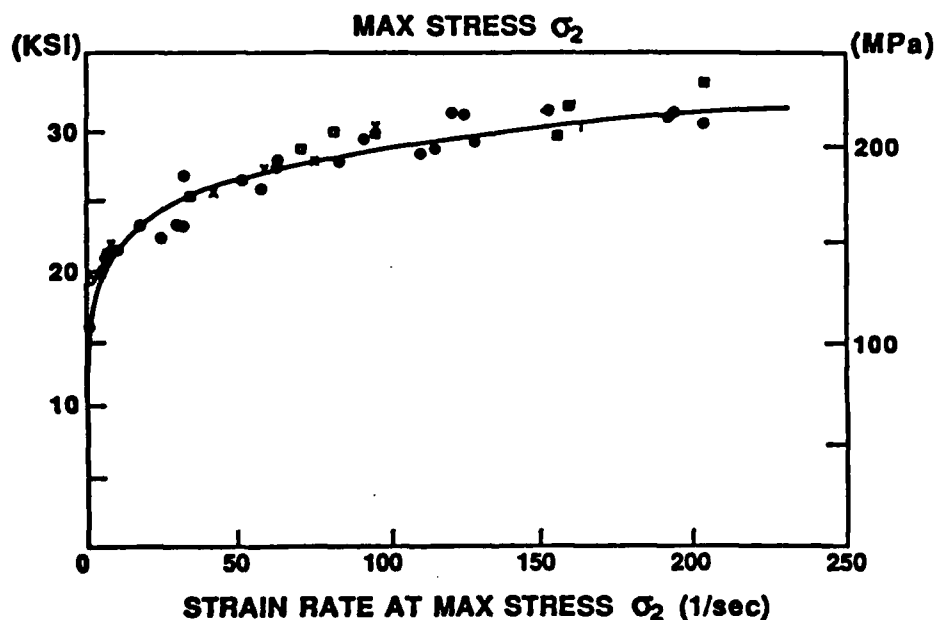

Figure 20.   Maximum Second Interface Stress Versus Strain Rate
for 32 SRI and 7 WES Specimens.

3.4.3 Slurry Infiltrated Fiber Concrete (SIFCON)

Unconfined dynamic compressive tests were performed on two groups of SIFCON specimens nominally 3 inches in diameter by 2.5 inches long, furnished by the New Mexico Engineering Research Institute (NMERI). Group 1 consisted of six specimens prepared earlier, while the main test group, Group 2, consisted of 10 specimens from a later batch which showed better dynamic strength properties. The SIFCON specimens required very high impact speeds of the Kolsky apparatus striker bar in order to get high stresses into the specimens, because of the low mechanical impedance of the SIFCON. The specimen ends were further ground at The University of Florida to obtain smoother and more nearly parallel surfaces.

Group 1 and Group 2 specimens performed quite differently in the dynamic tests. Figure 21 shows four of the dynamic stress-strain curves of Group 1 specimens, impacted at different speeds. The higher-speed impacts gave curves extending to higher strains. There is also a trend for the higher-speed impact curves to run at higher stresses, but this is not consistent. The highest stress reached with Specimen E at the lowest speed impact is almost the same as the maximum stress for Specimen F. The highest stress for Specimen E and the maximum stress for Specimen F are both higher than the maximum stress for Specimen C, despite the fact that Specimen C had the highest impact speed and the highest strain rate at the maximum stress. Except for Specimen E, the curves of Group 1 reach a maximum stress and then show a strain-softening regime, corresponding to shear failure.

Group 2 specimens (the main test group) did not fail (did not show a strain-softening regime) in the tests, except for one specimen. Permanent deformation was produced, and all but one of the curves show strain-hardening behavior similar to that of a ductile metal right up to the end of the test.
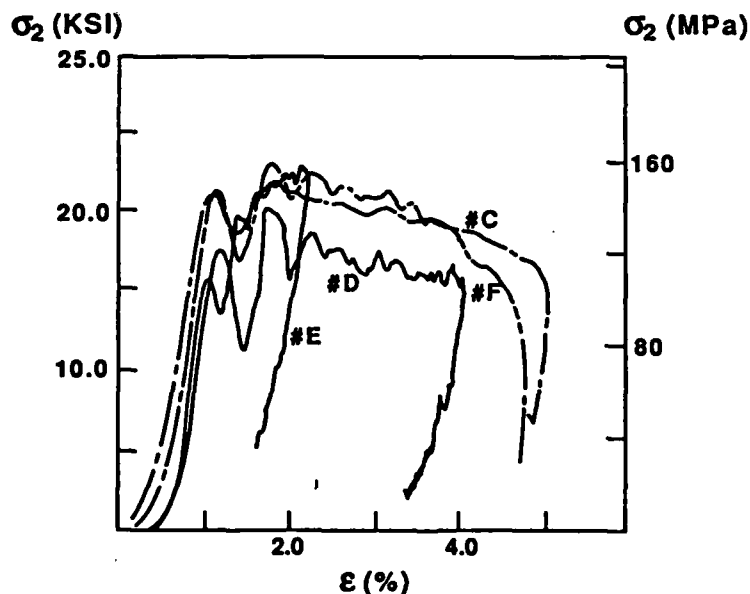

Figure 21. Dynamic Compressive Stress-Strain for
Four SIFCON Specimens of Group 1.

33

The end of the test was caused by the end of the 300 microsecond loading pulse and not by specimen failure. Four of the ten dynamic stress-strain curves of Group 2 are shown together in Figure 22. The "failure stress" results for Group 1, i.e. the maximum stress reached before the onset of strain softening showed only a slight upward trend versus the strain rate at the maximum stress, from 18.5 KSI at 83.2 sec^{-1} to 23.0 KSI at 159 sec^{-1}.
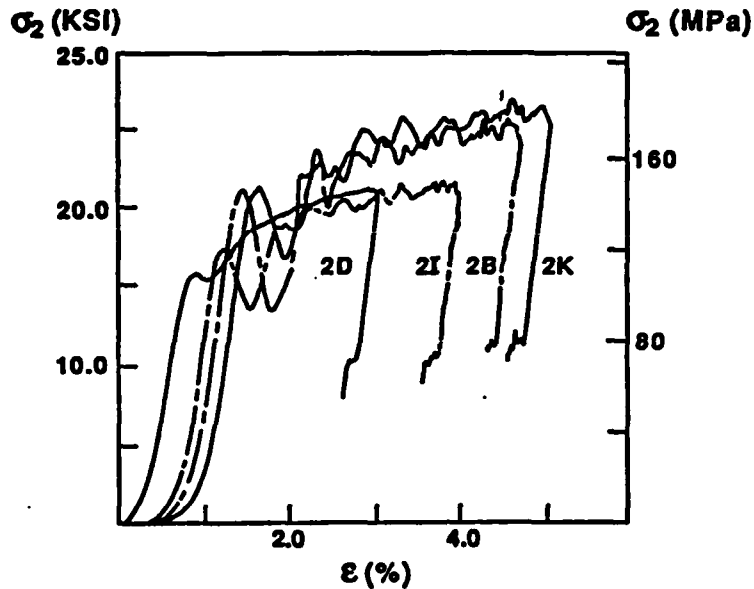

Figure 22. Dynamic Compressive Stress-Strain Curves
for Four SIFCON Specimens of Group 2.

Since the main test group did not reach this kind of failure in most cases, the rate-dependence was characterized by the stress at a strain of 3 percent versus the strain rate at that strain. There is a considerable amount of scatter, but over the strain-rate range from 50 sec^{-1} to 160 sec^{-1} the results show no rate dependence. Only one specimen of this group reached a strain-softening behavior after a maximum stress of 18.6 KSI at a strain of 4.69 percent and a strain rate at the maximum stress of 122.6 sec^{-1}.

Four of the Group 1 specimens showed noticeable shear bands, but only one of the Group 2 specimens did. All tested specimens remained intact. Lateral surfaces were roughened by the deformation, with some of the cementitious material at the surface loosened and many steel fibers protruding slightly. This surface roughening caused early failure of and/or irregular readings from surface strain gages. All the strain results presented in the figures are therefore based on the SHPB measurement and not on the surface strain measurements.

The stress values plotted were all based on the stress at the second interface of the specimen, which is considered to be more reliable than the first interface stress measurement. The maximum stress measurements are considered to be reliable, but with specimens this large the exact association of each stress with each strain in the curve is a little uncertain. SHPB strain measurement for SIFCON is further complicated by the lack of a good flat surface at the interface. The closing of this gap is measured as strain by the SHPB, which causes the strain measurements to be exaggerated.

34

3.5 Preliminary Results from Exploratory Studies

3.5.1 Dynamic Testing of Laterally Confined Concrete

The effect of lateral confinement on the axial dynamic stress-strain curves has been explored by placing metal jackets around the specimens. This was done first for a small number of mortar specimens in the small SHPB system. Results were so promising that a larger steel jacket was fabricated and a few tests have now been made on concrete in the larger SHPB system. The first results obtained with the larger system were not considered satisfactory, because the requisite initial snug fit between jacket and specimen was not achieved, so that the initial failures occurred with very little confinement. The approach has, however, produced some interesting results, and it is believed that with further optimization of the procedure some important information can be obtained about dynamic behavior under confinement.

Jacketed Mortar Specimens

Mortar specimens with thickness L = 0.4 inch and diameter D = 0.8 inch were coated with thick grease and placed inside an aluminum or steel cylindrical jacket of length 0.5 inch, which overlapped the 0.75-inch diameter pressure bars of the SHPB system by 0.05 inch on each end. Inside and outside diameters were:

	AL:	I.D. 0.832 inch	ST:	I.D. 0.834 inch
		O.D. 1.230 inch		O.D. 1.234 inch

Specimens were impacted at two different impact speeds, corresponding to drawbacks of 2.25 inch and 2.75 inch of the spring propelling the striker bar.

Figure 23 shows plots, for the two different impacts speeds, of stress σ and strain rate $\dot{\varepsilon}$ versus strain for specimens #2 and #3 confined by the steel jacket. Figure 24 shows results for Specimens #1 and #4 impacted at the same two speeds while confined by the aluminum jacket. Both jackets remained elastic, and, assuming that strains in the jacket do not vary in the axial direction, both the radial expansion of the inside boundary of the jacket and the confining pressure acting there were calculated for various times from the circumferential hoop strain data of the outside of the jacket, which was digitally recorded from strain gages mounted on the outer surface.

The first remarkable thing about these results is how reproducible they are as compared with the wide scatter noted in the unconfined tests on mortar. Figures 25 and 26 show the same results as Figures 23 and 24 except that two tests at the same speed but different jackets are shown in each figure. In Figure 25 (2.75-inch drawback) the axial stress-strain curve with the steel jacket almost coincides with that for the aluminum jacket, despite the fact that the confining pressure is higher with the steel jacket than with the aluminum jacket. The strain-rate versus strain curves are also close to each other. At the lower impact speed of Figure 26 the agreement is also good, although the curves diverge somewhat at the higher stresses.
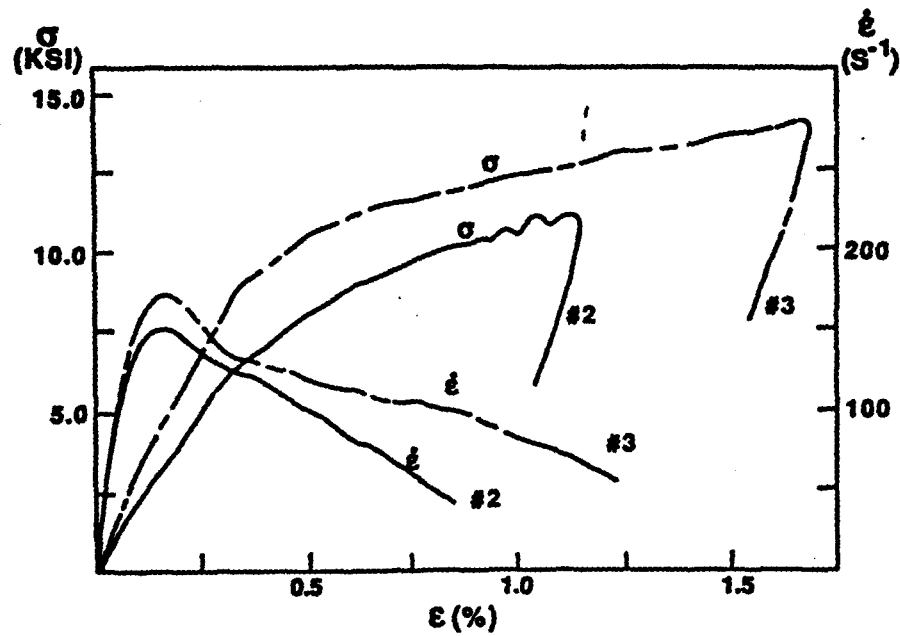
Figure 23. Stress and Strain Rate Versus Strain for
Steel-Jacketed Mortar Specimens #2 and #3
at Spring Drawbacks of 2.25 and 2.75 inches.
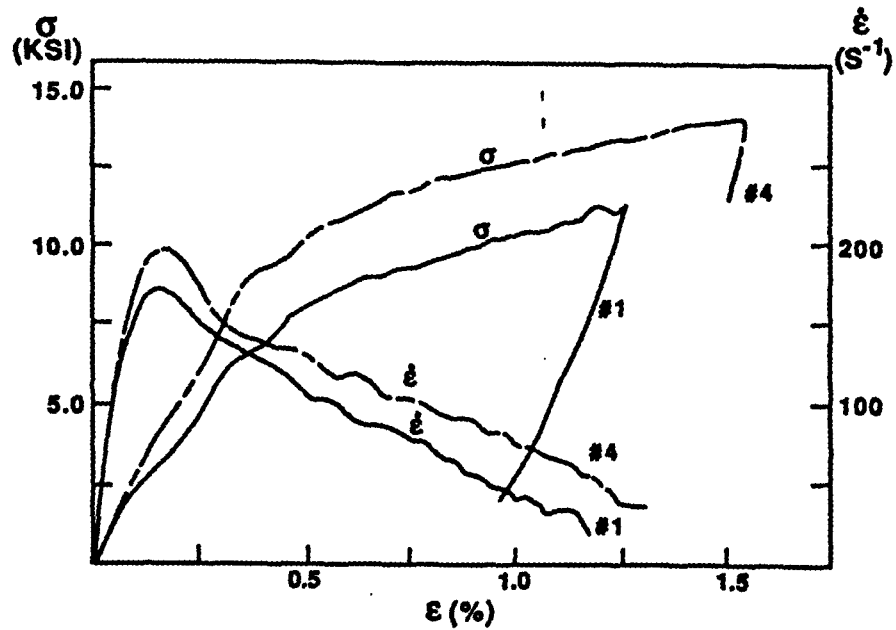

Figure 24. Stress and Strain Rate Versus Strain for
Aluminum-Jacketed Mortar Specimens #1 and #4
at Spring Drawbacks of 2.25 and 2.75 inches.
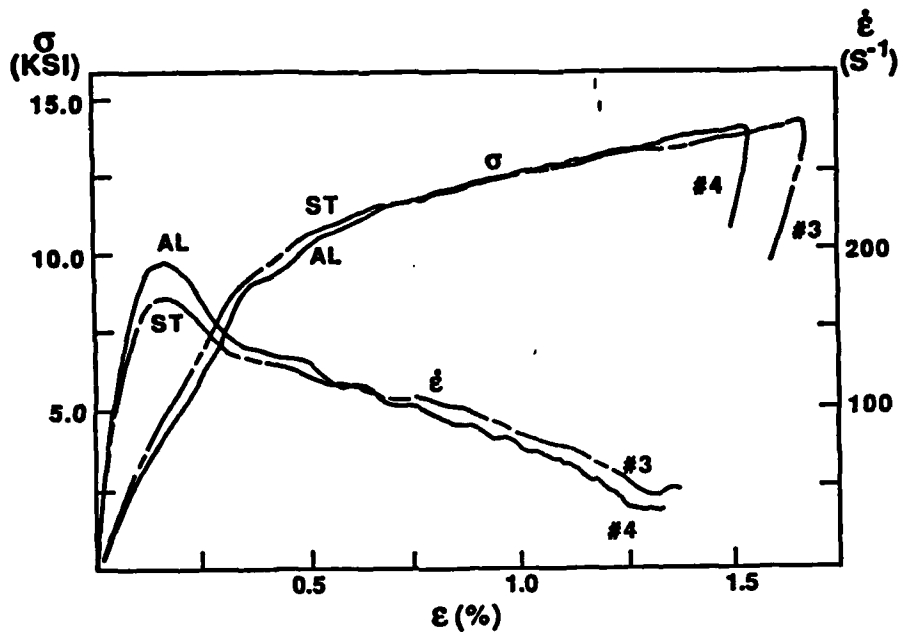
Figure 25. Steel-Jacketed Specimen #3 and Aluminum-
Jacketed Specimen #4 for Impacts with
Spring Drawback of 2.75 inches.
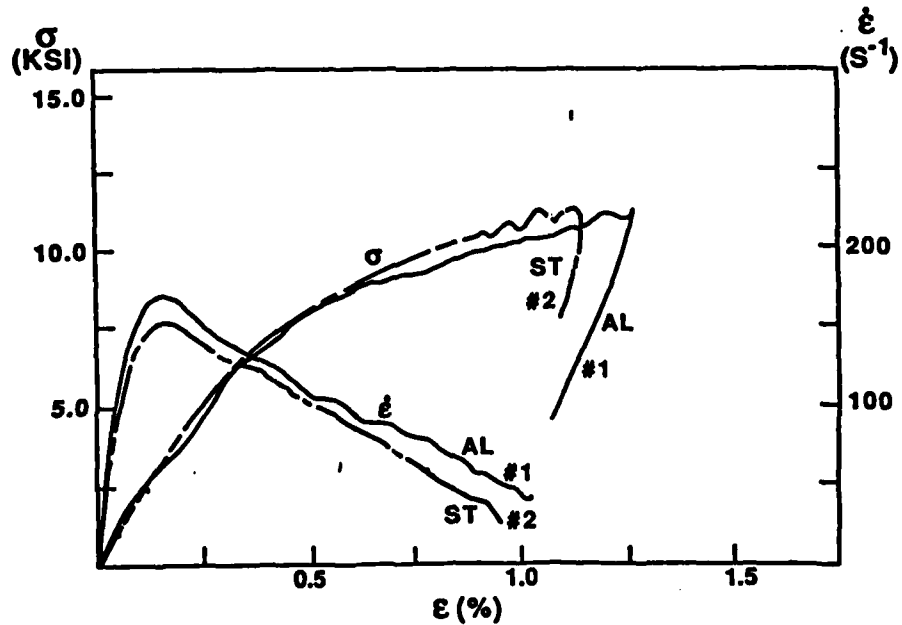
Figure 26. Steel-Jacketed Specimen #2 and Aluminum-
Jacketed Specimen #1 for Impacts with Spring
Drawback of 2.25 inches.

TABLE 3. SELECTED RESULTS FROM JACKETED TEST ON MORTAR

	2.25-inch drawback		2.75-inch drawback	
Jacket	AL	ST	AL	ST
Specimen	#1	#2	#4	#3
Strain 0.5 %				
Strain Rate (sec^{-1})	105.1	102.0	131.0	123.0
Stress (KSI)	8.03	8.12	10.1	10.6
pressure (KSI)	0.63	1.83	1.45	2.32
Strain 0.75 %				
Strain Rate (sec^{-1})	76.7	61.5	103.6	108.3
Stress (KSI)	9.30	9.78	11.7	11.7
pressure (KSI)	0.86	1.19	1.89	3.18
Strain 1.0 %				
Strain Rate (sec^{-1})	39.6	20.9	75.3	85.1
Stress (KSI)	10.3	10.7	12.6	12.6
pressure (KSI)	2.51	2.05	2.2	4.17

Table 3 summarizes some of the numerical results for the axial strain rate, axial stress and confining pressure in the different tests at selected strain levels. The comparison of AL and ST at 2.75-inch drawback shows that the stiffer steel provided consistently higher confinement than the aluminum at the same strain, although the stresses are about the same where the strain rates do not differ much. For the lower speed test at 2.25-inch drawback the steel confinement starts out higher than the aluminum but drops off at 1 percent strain near the end of the test. In these confined tests, the end of the test is controlled by the length of the loading pulse rather than by specimen failure. The specimen does not break up as in an unconfined test, but gives a stress-strain curve like a ductile metal, at least over the range of strains attained during the length of the applied loading pulse.

The higher confining pressure provided by the steel jacket at the 2.75-inch drawback in Figure 25 and up to an axial strain of 0.75 at the lower speed impact of Figure 26 did not cause a significantly higher stress-strain curve with the steel jacket.

Comparisons at the two speeds with the same jacket (Figures 23 and 24) show a significantly higher axial stress-strain curve at the higher speed. This was at first thought to indicate a significant strain-rate effect in the confined tests, but closer examination makes this conclusion uncertain. For Figure 24 the percentage changes in axial strain rate, axial stress and confining pressure from the lower curve to the higher curve at the selected strains are as shown in Table 4. Similar changes occur also in Figure 23.

38

TABLE 4.   CHANGES FROM #1 TO #4 IN FIGURE 24.

PERCENTAGE CHANGES IN

AT STRAIN	STRAIN RATE	STRESS	PRESSURE
0.5 %	25	26	82
0.75 %	35	21	120
1.0 %	40	22	-12

It thus appears that there was a significant increase in confining pressure exerted by the jacket at the higher speed (except near the end of the test). Thus, the increase in axial stress may be partly attributable to increase in confining pressure instead of to increase in strain rate. This would, however, contradict the comparison already noted for Figure 25, where the 60 to 90 percent higher pressure with the steel jacketed specimen #3 as compared with the aluminum jacketed specimen #4 did not result in a significantly higher stress-strain curve at the same impact speed and very nearly the same strain rates.

Data for two tests with the same confining pressure but significantly different strain rates, which would unambiguously verify a pure strain rate effect in the confined tests have not been obtained. Such data might be obtainable with a hydraulic radial confining pressure on a specimen surrounded by a thin membrane.

Jacketed Concrete Specimens

The results on mortar were so promising that a larger steel jacket was fabricated, and several tests have been made with it on concrete specimens prepared at the University of Florida. The initial results are not considered satisfactory. The jacket was 3.5 inches long, so that with a specimen 3 inches long the jacket overlaps the pressure bars 0.25 inches at each end. In order to avoid interference with the 3-inch diameter pressure bars, the jacket was made with inside diameter 3.01 inches, but this is too large for the 3-inch diameter specimens that were available, which were cast in 3 x 6 inch carton molds.

Figure 27 shows stress-strain curves for five specimens of a plasticized concrete prepared at the University of Florida, which were tested in this jacket at five different impact speeds. (The curves are labeled with the firing pressures in the gas gun that propelled the striker bar.) The initial peaks on all except the lowest-speed case are essentially unconfined dynamic strengths because the jacket was so loose. These dynamic strengths are significantly higher than the static unconfined compressive strengths (5.5 to 6.4 KSI) measured on specimens of the same size. Examination of time traces for six tests of this kind showed that there was a time delay averaging about 75 microseconds before the beginning of the signal from the strain gages mounted on the outer wall of the jacket (as compared with the time the signal begins from strain gages mounted directly on an unconfined specimen). Most of this delay is associated with the closing of the initial gap between the specimen and jacket.
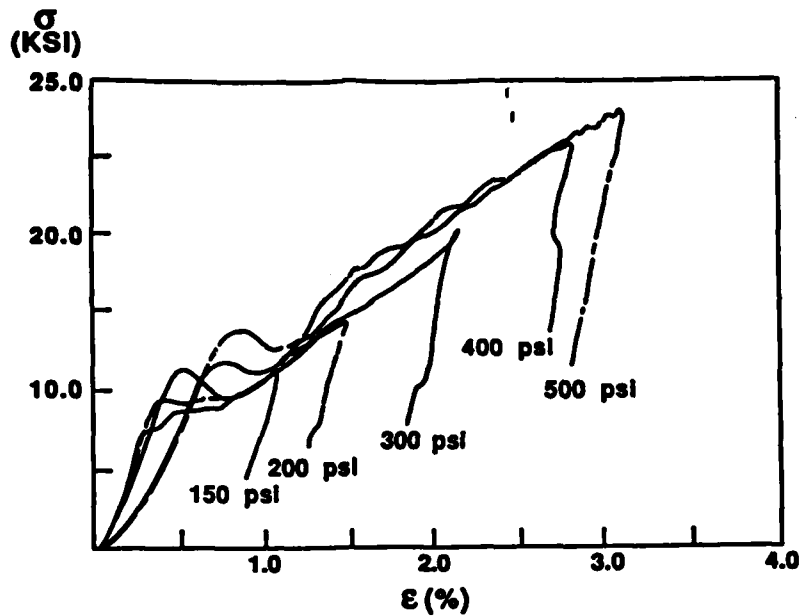
Figure 27.   Stress-Strain Curves for Five Steel-Jacketed
             Concrete Specimens.   (Curves are labeled with the
             gas-gun firing pressures.)

After the initial peaks in Figure 27, expansion of the specimen as it
continues to deform axially causes expansion of the jacket, inducing confining
pressure exerted by the jacket, and a strain hardening regime occurs for the
further dynamic compression.

New molds for casting the concrete were fabricated from aluminum cylin-
ders with inside diameter 3.01 inches, providing specimens with a tighter fit
in the jacket, so that in two preliminary tests the delay time was reduced
from 75 microsec to about 26 microsec. It should be possible to reduce the
delay even more.

Specimens with inside diameter 3.01 inches and length 2 inches were cut
from bars cast in the new molds. Confined dynamic compressive tests on a few
of the new specimens were run in the old steel jacket (3.5 inches long) and a
new aluminum jacket (2.4 inches long). Stress-strain and strain-rate versus
strain curves are shown in Figure 28 for two specimens tested with the same
gas gun firing pressure of 200 psi, one in the steel jacket and one in the
aluminum jacket. No drop in stress after the apparent yield point is noted.
The aluminum-jacket curves run slightly above the steel curves. Apparent
confining pressures were about the same for the two jackets, which was
surprising in view of the higher modulus of the steel. It was suspected that
the assumed lack of axial uniformity in the elastic deformation of the steel
jacket was not adequately realized because the steel jacket was so much longer
than the expanding specimen, so that the pressure calculation may have been in
error. It is also possible that the aluminum jacket may have undergone some
plastic deformation, so that the actual internal pressure may have been less
than that calculated based on assumed elastic response of the jacket.

40
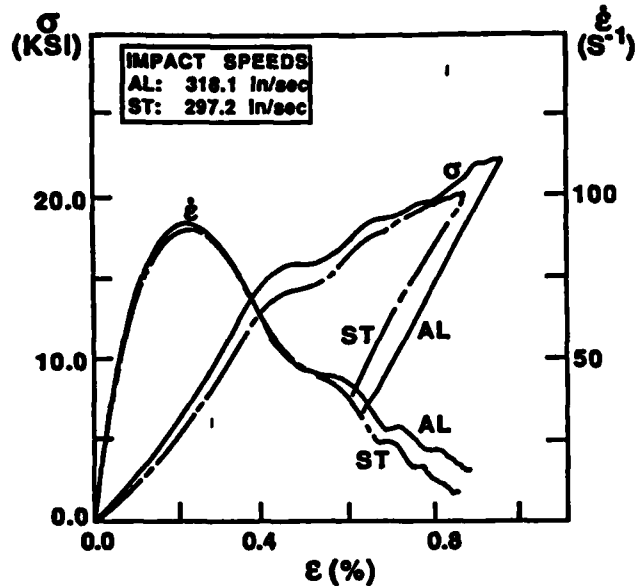
Figure 28.   Stress-Strain Curves and Strain Versus Strain Rate Curves
             for a Steel-Jacketed Specimen and an Aluminum-Jacketed
             Specimen Impacted at Approximately the Same Speed.

Further refinement of the technique is needed. It is believed that with these refinements results similar to those on mortar will be obtained for concrete, and that a systematic investigation can furnish useful information about the response of concrete confined by surrounding material.

3.5.2 Delayed Failure in Unconfined Tests at Low Impact Speeds

Figure 29 shows the second-interface stress and and specimen strain rate versus time as determined with the large SHPB system on a WES limestone-aggregate specimen. The curve is marked with a point 1, which may be considered as a sort of yield point, and a point 2 where strain softening begins is also marked. Yield point determination will be discussed later. In Figure 29, stress and strain rate are almost constant between the two points. In the other similar tests the constancy is more approximate, but there is an extensive period where the stress increases slowly.

In Figure 30 the results for similar observations on 14 specimens are summarized. The Max σ_2 Duration, the time between point 1 and point 2, is plotted as abscissa and the Max σ_2 as ordinate. The waiting time before the onset of strain softening increases with decreasing maximum stress, although little data is available for the longer times. At still higher impact speeds, point 2 approaches point 1 and the waiting time approaches zero.

41
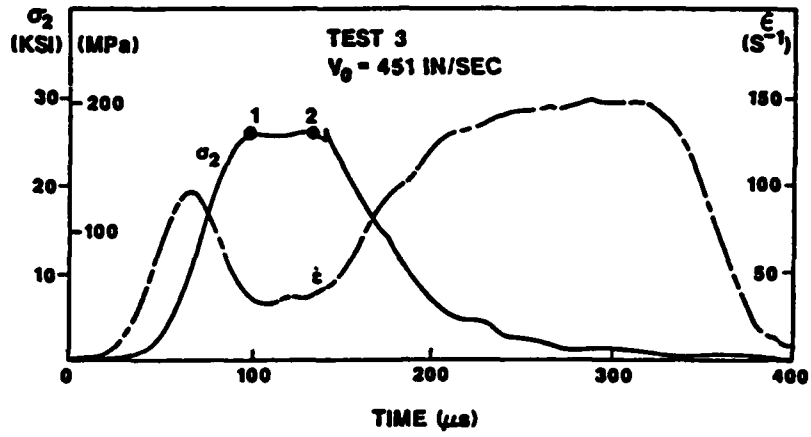
Figure 29. Stress and Strain Rate in WES Specimen Showing
Yield Point 1 and Onset of Strain Softening 2.
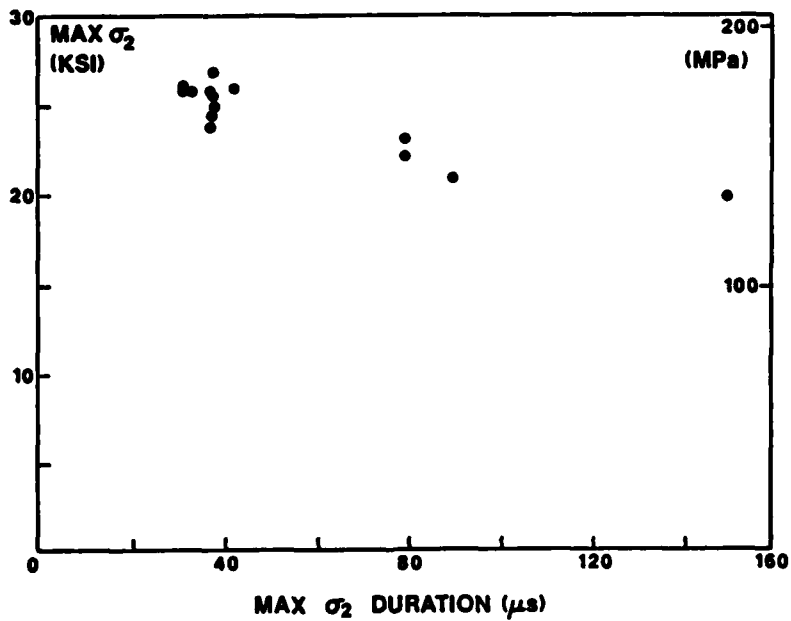
Figure 30. Maximum Stress Versus Duration of Waiting Time
Between Yield and Onset of Strain Softening.

42

One specimen not included in this plot sustained a stress of 19.2 KSI for about 240 microseconds without any visible damage. The duration of 240 microseconds was controlled by the length of the applied loading pulse (300 microseconds minus the rise time of about 60 microseconds) and not by the onset of strain softening, which did not occur in this case. It is conjectured that the specimen would have failed eventually if the loading pulse had been longer, since the static unconfined strength in our measurements was between 13 KSI and 17 KSI. This suggests the existence of a delay time in the onset of microcrack development, as contrasted with the results of Figure 30, which show an additional waiting period between the onset of microcrack development and the time when the microcrack development leads to general failure and strain softening. Figure 31 shows that the additional strain increment developed during this time is roughly independent of the strain rate during the waiting time. Higher stress gives a higher strain rate but for a shorter time.

The initiation delay time needs further investigation. The SHPB system can be modified to accommodate a longer striker bar that will provide a longer loading pulse. The initiation delay time as a function of the applied stress level could then be determined systematically. The initiation delay time cannot be attributed to lateral inertia confinement of the specimen, since during the constant maximum stress period before initiation of permanent deformation there is no deformation, and there is zero lateral inertia. The presence of the initiation delay time gives rise to an apparent strain-rate effect, since a stress higher than the static ultimate strength is sustained. Then, when permanent deformation finally begins, it begins at a higher rate when the stress reached was higher.
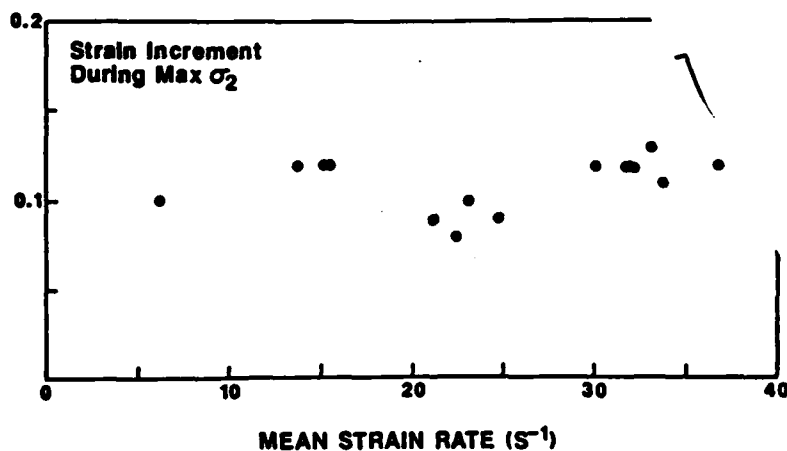

Figure 31. Strain Increment During Waiting
Time Versus Strain Rate.

The waiting times between points 1 and 2, summarized in Figures 30 and 31, are damage accumulation times. The damage accumulation time also contributes to the apparent strain-rate effect, but in this regime the apparent rate effect could be partly attributable to lateral inertia confinement of the interior of the specimen, since it is well known that in quasistatic tests lateral confining pressure leads to enhanced axial strength and ductility. Yield points for eight specimens were determined by a procedure discussed in the following subsection. The other six were estimated at bend points in the stress-strain curve.

3.5.3 Lateral Inertia Estimation in Unconfined Tests

Both axial and circumferential hoop strain gages were mounted on nine specimens. Analysis of the hoop strain versus time record furnished information about the lateral acceleration of the surface and made possible an estimation of the lateral inertia confinement.

Plots of the surface hoop strain ε_θ versus axial strain ε_z were approximately linear, indicating an approximately constant Poisson's ratio of about 0.25, up to a bend point, which was taken as indicating "yield." The bend point was quite sharp at most impact speeds, but a little less sharp at the highest speeds.
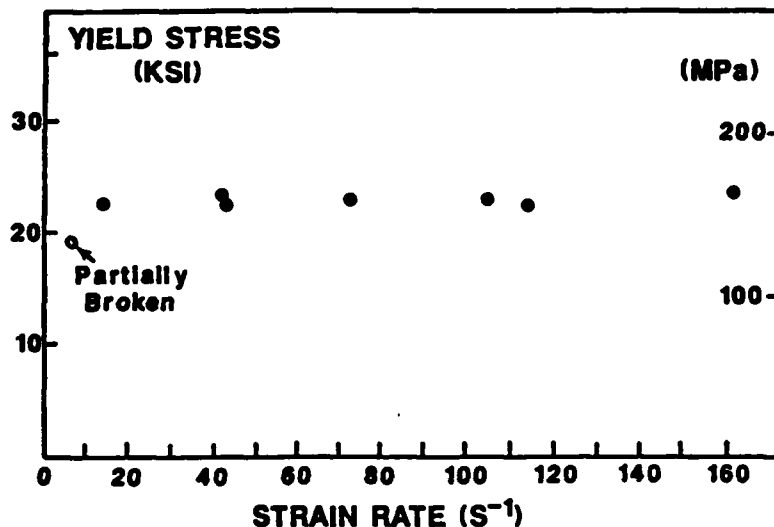
Figure 32. Yield Stress Versus Strain Rate at Yield.

Figure 32 is a plot of the yield stress at the yield point so determined versus the strain rate at the yield point for eight specimens. It shows that the yield stress, as determined in this way, is approximately independent of strain rate over this range of dynamic rates, although these dynamic yield stresses are all higher than the static ultimate strengths of 13 to 17 KSI.

It has been suggested that the enhanced dynamic strength is a consequence of the lateral inertia confinement of the interior. The lateral inertia and the radial stress induced by it were estimated as follows. Shear stresses were assumed negligible, and the specimen deformation was assumed uniform. Then the radial strain and hoop strain are equal and independent of the

44

distance r from the centerline and can be determined by the surface measurement of hoop strain. The radial displacement u at radial coordinate r is given by

$$u = r\varepsilon_\theta \qquad (25)$$

which can be substituted into the radial equation of motion,

$$\frac{\partial \sigma_r}{\partial r} = \rho \frac{\partial^2 u}{\partial t^2} \qquad (26)$$

to give

$$\frac{\partial \sigma_r}{\partial r} = \rho \ddot{\varepsilon}_\theta r \qquad (27)$$

whence

$$\sigma_r = -\frac{1}{2} \rho \ddot{\varepsilon}_\theta R^2 [1 - (r/R)^2] \qquad (28)$$

where R is the outside radius where the surface strains are measured. Equation (28) was used to estimate the confining pressure $|\sigma_r|$ at various values of r/R for the nine strain-gaged specimens. Two regimes were considered: before yield and between yield point and maximum stress.

Before Yield the Poisson's ratio was approximately constant, and the estimation procedure is most reliable. In this regime the the second time derivatives of the hoop strain were calculated from the relationship $\dot{\varepsilon}_\theta = -\nu\dot{\varepsilon}$ where $\dot{\varepsilon}$ is the axial strain rate from the SHPB records, since the SHPB strain rates were directly recorded and were much smoother than the differentiated hoop strain records. In this regime the lateral inertia confinement values of $|\sigma_r|$ were estimated in two ways:

(1) by using the average $\ddot{\varepsilon}$ from the start to the point of maximum $\dot{\varepsilon}$, and

(2) by using the average $\ddot{\varepsilon}$ from the start to the yield point.

The first method gave higher values during the early elastic part of the regime where the strain rate was increasing most rapidly. Both methods should overestimate the actual lateral inertia confinement at the yield point, since the strain acceleration at the yield point is lower than the average values up to that point. Plots of the confining pressure versus r/R, estimated by the first method for 9 specimens are given in Figure 33. The maximum confining pressure occurs at r = 0, and the maximum value estimated there for the highest impact speed (firing pressure 600 psi) was 291 psi, which is not significant compared to the static unconfined strength (13,000 to 17,000 psi) and therefore cannot be considered to be the cause of the enhanced dynamic yield stresses shown in Figure 32.

Between Yield and Maximum Stress the apparent Poisson's ratio is not constant, and it would be necessary to differentiate the hoop strain rate record twice to obtain the hoop strain acceleration. Instead of doing this numerically it was decided to estimate the average hoop strain acceleration during intervals where the hoop strain rate records, obtained by numerical differentiation of the recorded hoop strains followed by smoothing, were approximately linear. In this regime, plots of estimated lateral inertia

45

confining pressure versus r/R have the same shape as those of Figure 33 but different magnitudes. The nine gaged specimens were divided into two groups. Group 1 included seven specimens which exhibited a waiting time or delayed failure between yield and the onset of strain softening. Unfortunately usable strain-gage data during the waiting time were obtained from only three of the seven specimens.
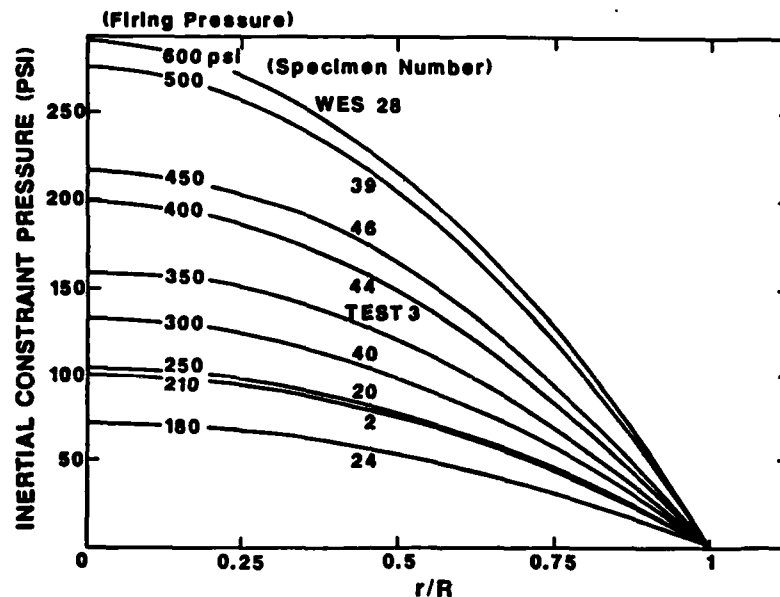

Figure 33. Lateral Inertial Confinement Pressure Versus r/R
Based on Average Hoop Strain Acceleration Between
Beginning and Time of Maximum Axial Strain Rate.

For these three, ε_θ was taken as the change $\Delta\dot{\varepsilon}_\theta$ divided by the time Δt over which the $\ddot{\varepsilon}_\theta$ record was approximately linear. The highest inertial confinement estimated in this regime was less than 600 psi at the center and less than 300 psi at r = 3R/4.

Group 2 included the two specimens tested at the highest impact speeds, where there was no delayed failure. For this group the recorded hoop strain rate increased approximately linearly from the time of maximum axial strain rate to the time of maximum second interface stress σ_2 and then changed to another approximately linear interval up to about the time of the maximum first interface stress σ_1. For the regime after the maximum σ_2, the maximum estimated confining pressure is 3410 psi at the center and 2550 psi at r = R/2, which could significantly enhance the apparent dynamic strength.

Summary and Conclusions of Task II are presented in Section 4.2.

SECTION IV

SUMMARY AND CONCLUSIONS

4.1 Summary and Conclusions of Task I

Several methods have been presented in Section II for prediction of
concrete and reinforced concrete direct shear failure at a position away from
edges of the slab or beam. All three methods indicate similar results but
details of reinforcing arrangement, which appear to have significant effects
on response modes, are difficult to model. Current tests of air blast on
reinforced slabs indicate that the addition of shear reinforcement or stirrups
tends to increase damage. Apparently the additional through-the-thickness
reinforcement may add an additional stress riser which reduces the shear
strength or shear resistance to localized loads. This means that measures to
increase the flexural strength or resistance of a structure may tend to weaken
it relatively for localized shear resistance. This argument tends to support
a model similar to that of Eq. (18). However, tests of very close-in or
contact explosives show steel reinforcing failure immediately beneath the
explosive. It is probably more reasonable to assume that a combination of
response failure models would be more appropriate, but it is not clear as to
the time sequence of application of such models. These observations simply
point out the lack of understanding of the response and subsequent failure of
concrete and reinforced concrete when subjected to very dynamic localized
loadings.

With these thoughts in mind and the uncertainty of prediction of the
loading from buried explosives, no changes were made to the existing
predictive model REICON of Reference (7). This model in its current form, on
file in the Computing Center at Eglin AFB, Florida, contains a flexural
response subroutine based on fixed and moving plastic hinges or yield lines
and a subroutine for the shear response model of Eqs. (8) and (9). It was
concluded that, until a better understanding of the shear failure process was
available, the critical impulse model was adequate.

The continued effort to use the finite element code NONSAP-C for predic-
tion of onset of localized failure is not justified. However, the resulting
strain rate data of Table 2 appears useful in that it does indicate that
strain rates for structural response of concrete slabs are in the low range of
1 to 25 except at points very close to the intense loading.

The overall general conclusion for direct localized shear is that a clear
understanding of this phenomenon is not yet available, but simple single
degree of freedom models with proper logic are better predictors than exten-
sive finite element codes. Finite difference code methods could be used, but
they appear to be too expensive for modeling of general structural response of
reinforced concrete systems.

It is recommended that a series of tests designed specifically to examine
the localized direct shear response be conducted. These tests should be lab-
oratory in nature with very close control and variations of parameters such
explosive, slab thickness, concrete tensile and compressive strength, rein-
forcement quantity, quality, and strength. These tests should be well
instrumented to measure external and internal strains, through-the-thickness

wave propagation, slab velocities and accelerations. Also high speed camera coverage should be available to record over-all response. It will be necessary to give some thought to methods of preventing dust and debris from masking the camera view.

4.2 Summary and Conclusion of Task II

1. The Kolsky apparatus or Split Hopkinson's Pressure Bar system is a useful tool for determining the dynamic ultimate compressive strength of concrete, at least at the moderate impact speeds leading to failure strain rates below about 120/sec.

2. The larger specimen and larger-diameter pressure bars, however, introduce two problems. For longer specimens the desired degree of uniformity along the length is not achieved. For example, with specimens 2.6 inches long the possible error in stress measurement at an average strain of 0.004 was estimated to vary from about 2 percent at low impact speeds to 5 percent at moderate speeds and 18 percent at the highest speeds in the test series. The error was smaller at the maximum stress (1 to 5 percent) but larger at smaller strains where the stress was changing rapidly--as much as 40 to 50 percent possible error at a strain of 0.002. Maximum stresses are still reasonably well measured, but the stress-strain curve determination involves some uncertainty about what stress to associate with the average strain at each instant. The larger diameter also leads to more noticeable Pochhammer-Chree radial oscillations in the incident pressure bar, which interfere with the interpretation of the longitudinal strain measurement in the incident pressure bar and hence interfere with the force and displacement recording at the specimen's incident bar interface. Despite these problems, the SHPB system appears to be the best available system for determining dynamic compressive properties in the moderately high deformation rate range.

3. Unconfined dynamic compressive tests on five kinds of high-strength concrete have shown significant apparent strain-rate effects, leading to dynamic ultimate strength as much as twice the static value at failure strain rates of the order of 100/sec, as reported in Section 3.4.2.

   The following tentative conclusions are based on a limited number of tests, specifically nine tests on one kind of concrete.

4. Within the range of dynamic loading rates applied to these nine unconfined specimens the deformation appears to divide into three regimes:

   A. An essentially elastic regime with constant apparent Poisson's ratio up to a yield stress where the apparent Poisson's ratio begins to increase as significant microcrack extension begins. The yield stress appears to be independent of the strain rate at yield, although all the dynamic yield stresses observed were at least 30 percent higher than the static ultimate strength. Low-speed impacts with longer loading pulses might show lower yield stresses. The enhanced dynamic yield strength cannot be attributed to lateral inertia confinement.

   B. A regime of of significant microcrack extension (and possibly new crack initiation) in which the average stress and strain rate in the specimen may remain approximately constant up to the beginning of apparent strain softening. The strain accumulation during this waiting period

between yield and strain softening appears to be independent of the strain rate. As the strain approaches the failure strain, lateral inertia confinement becomes significant, especially at the higher speeds of impact. As the impact speed increases, the duration of this regime shrinks to zero.

C. The strain softening regime in which we have almost no observations beyond the pressure-bar data. In a few cases a strain gage continued to function on a fragment that had been split off from the specimen and unloaded.

5. The rate-independent strain accumulation between yield and failure (see 4-B) suggests that a rate-independent strain criterion for failure might be formulated, which would imply a rate-dependent stress condition.

6. A damage accumlation model seems appropriate for the regime between yield and failure, but all this needs much more investigation.

7. Further study of lateral inertia confinement effects and of the dynamic response of passively confined concrete specimens is needed. Alternative measurement methods should be explored. A high speed camera that could take at least 20 to 30 exposures during the 200 to 300 microsecond event would furnish useful information on the overall deformation process and could give information about the lateral accelerations beyond the maximum stress where gages usually fail. This requires an interval between exposures that can be set as short as 10 microseconds or preferably even shorter.

Two dimensional (radially symmetric) analysis of the deforming specimen can be made, based on various assumed constitutive models for the concrete. Such computations can be checked against the measured surface strain records without the assumption of longitudinally uniform deformation of the specimen.

SECTION V

REFERENCES

1. Malvern, L. E. and Ross, C. A., "Dynamic Response of Concrete and Concrete Structures," First Annual Technical Report, AFOSR Contract F49620-83-K007, Jan. 1984.

2. Malvern, L. E. and Ross, C. A., "Dynamic Response of Concrete and Concrete Structures," Second Annual Technical Report, AFOSR F49620-83-L007, Feb. 1985.

3. Osburn, J. J., "Hydrocode Calculations of High Length-to-Diameter Cylindrical Explosions in Sand," AFATL-TR-82-10 Air Force Armament Laboratory, Eglin AFB, FL, Feb. 1982.

4. Cook, W. H., "Sand/Concrete Wave Reflection Calculations," University of Florida Independent Study Project, Eglin Graduate Center, Eglin AFB, FL, July 1984.

5. Daniel, I. M., "Photoelastic Study of Wave Propagation in Layered Media," AFWL-TR-68-153 Air Force Weapons Laboratory, Kirtland AFB, NM, July 1969.

6. Drake, J. L., and Little, C. D., Jr., "Ground Shock from Penetrating Conventional Weapons," Symposium Proceedings of The Interaction of Non-Nuclear Munitions With Structures, US Air Force Academy, CO, May 1983.

7. Ross, C. A., Sierakowski, R. L., and Schauble, C. D., "Concrete Breaching Analysis," AFATL-TR-81-105, Air Force Armament Laboratory, Eglin AFB, FL, December 1981.

8. Ross, C.A. and Rosengren, P.L.,Jr., "Expedient Nonlinear Dynamic Analysis of Reinforced Concrete Structures," Proc. Second Symposium on the Interaction of Non-Nuclear Munitions with Structures, Panama City Beach, FL, 15-19 April 1985, pp 45-51.

9. Ross, T. J., "Direct Shear Failure in Reinforced Concrete Beams Under Impulsive Loading," AFWL-TR-83-84 Air Force Weapons Laboratory, Kirtland AFB, NM, September 1983.

10. Slawson, T. R., "Dynamic Shear Failure of Shallow Buried Flat-Roofed Reinforced Concrete Structures Subjected to Blast Loading," TR SL-84-7 USAE Waterways Experiment Station, Vicksburg, MS, April 1984.

11. Jones, N., "Plastic Failure of Ductile Beams Loaded Dynamically," Trans. ASME Vol. 98 Series B No. 1, Feb. 1976, pp. 131-136.

12. Zukas, J. A., Nicholas, T., Swift, H. F., Greszczuk, L. B., and Curran, D. R., Impact Dynamics, Wiley-Interscience, New York, NY, 1982, p. 318.

13. Matlock, A. H. and Hawkins, N. M., "Shear Transfer in Reinforced Concrete - Recent Research," Portland Cement Institute Journal, March-April, 1972.

14. Smith, P. D. and Anderson, C. A., "NONSAP-C: A Nonlinear Stress Analysis Program for Concrete Containments Under Static, Dynamic, and Long-Term Loadings," Los Alamos National Laboratory Report NUREG/CR-0416, October 1978.

15. Malvern, L. E., Tang, T. and Jenkins, D. A., "Dynamic Compressive Testing of Concrete and Mortar," Engineering Mechanics in Civil Engineering, Vol. 1, eds. A. P. Boresi and K. P. Chong, pp. 663-666, ASCE, NY, 1984.

16. Malvern, L. E., Jenkins, D. A. Tang, T. and Ross, C. A., "Dynamic Compressive Testing of Concrete," in Proc. Second Symposium on The Interaction of Non-Nuclear Munitions with Structures, Panama City Beach, Florida, April 1985, pp. 194-199.

17. Malvern, L. E., Tang, T., Jenkins, D. A. and Gong, J. C., "Dynamic Compressive Strength of Cementitious Materials," Cement-Based Composites: Strain Rate Effects on Fracture (ed. S. Mindess and S. P. Shah), Symposium S, Boston, Dec. 1985, Materials Research Society Symp. Proceedings, Vol. 64 (in press 1986).

18. McHenry, D. and Shideler, J.J., "Review of Data on Effect of Speed in Mechanical Testing of Concrete," ASTM STP 185, pp 72-82, 1956.

19. Watstein, D., "Effect of Straining Rate on the Compressive Strength and Elastic Properties of Concrete," ACI Journal, Vol 24, 729-744, 1953.

20. Kolsky, H., "An Investigation of the Mechanical Properties of Materials at Very High Rates of Loading," Proc. Phys. Soc. (London) Ser B, Vol 62, pp 676-704, 1949.

21. Lindholm, U.S., "Some Experiments with the Split Hopkinson's Pressure Bar," J. Mech Phys. Solids, Vol 12, 317-335, 1964.

22. Nicholas, T. in Impact Dynamics, eds. Zukas et al., John Wiley and Sons, New York, 1982, pp 277-332.

23. Bhargava, A. & Rehnstrom, A., "Dynamic Strength of Polymer Modified and Fiber-Reinforced Concretes," Cement and Concrete Research, Vol 7, pp 199-208, 1977.

24. Kormeling, H.A., Zielinski, A.J., and Reinhardt, H.W., "Experiments on Concrete Under Single and Repeated Impact Loading," Report No. 5-80-3, Delft University of Technology, Stevin Laboratory, May 1980.

25. Suaris, W. and Shah, S.P., "Mechanical Properties of Materials Subjected to Impact," RILEM-CEB-IABSE-Interassociation Symposium on Concrete Structures Under Impact and Impulsive Loading, Berlin, 1982, pp 33-62.

26. Shah, S.P., "Concrete and Fiber Reinforced Concrete Subjected to Impact Loading," in Cement-Based Composites: Strain-Rate Effects on Fracture (ed. S. Mindess and S.P. Shah) Materials Research Society Symposium S, Boston, Dec. 1985, Symposium Proc. Vol. 64 (in press 1986).

27. Glenn, L.A. and Janach, W., "Failure of Granite Cylinders Under Impact Loading," Intl. J. of Fracture, Vol 13, pp 301-317, 1977.

28. Young, C. and Powell, C.N. "Lateral Inertia Effects on Rock Failure in Split Hopkinson-Bar Experiments," 20th U.S. Symposium on Rock Mechanics, 1979.

29. Bertholf, L.D. and Karnes, C.H., "Two-dimensional analysis of the split Hopkinson pressure bar system," J. Mech. Phys. Solids, Vol 23, 1-19, 1975.

30. Follansbee, P. S. and Frantz, C., "Wave Propagation in the Split Hopkinson Pressure Bar," ASME Journal of Engineering Materials and Technology, Vol. 105, pp. 61-66, 1983.

END

12-86

DTIC